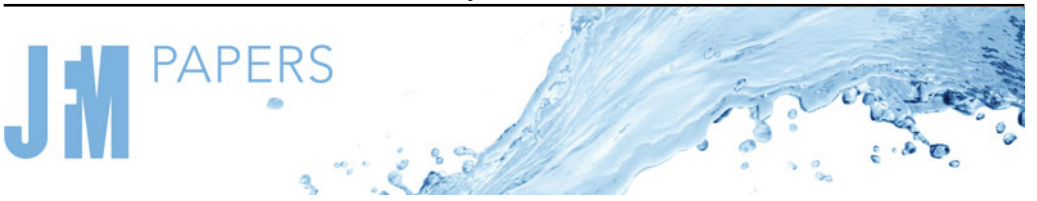
Check for updates

*J. Fluid Mech.* (2026), *vol.* 1044, A25, doi:10.1017/jfm.2026.12085




# Response of a turbulent boundary layer to a synthetic periodic large-scale structure

**Mitchell Lozier**[1], **Flint O. Thomas**[1] **and Stanislav Gordeyev**[1]

[1]Department of Aerospace and Mechanical Engineering, University of Notre Dame, Indiana 46556, USA

**Corresponding authors:** Mitchell Lozier, lozier.me@gmail.com; Stanislav Gordeyev, sgordeye@nd.edu

(Received 25 September 2025 UTC; revised 31 August 2026 UTC; accepted 31 August 2026 UTC)

The dynamic response of a zero-pressure-gradient turbulent boundary layer (TBL) to a large-scale perturbation in the outer region was investigated experimentally. The baseline TBL had a moderate Reynolds number such that there were no naturally occurring energetic large-scale structures (LSS) present. An active plasma-based actuator was then placed in the outer region of the TBL to introduce a periodic, spanwise-uniform, synthetic LSS. Thus this novel actuation scheme provides a new tool by which to experimentally examine an idealised case of outer–inner layer interaction within the TBL. The TBL response to this synthetic LSS was investigated using a combination of planar particle image velocimetry and spanwise offset hot-wires, over a large streamwise extent downstream of the actuator device. Phase-locked analysis was implemented to isolate and measure the streamwise development of the imposed synthetic LSS and resulting phase-dependent changes in turbulence amplitudes throughout the TBL. A strong correlation was observed between large-scale motions near the wall, which were found to be linearly superimposed from the outer-region synthetic LSS, and a periodic modulation of the turbulence amplitude. Further, this periodic modulation was found to be linked to phase-dependent changes in both the production and transport of turbulence driven by the induced streamwise and wall-normal large-scale motions. The phase speed of these induced large-scale motions, coupled with intermittent changes to spanwise coherence near the wall, also revealed a clear, but transient, effect of the outer-region synthetic LSS on the near-wall cycle dynamics. Overall, these results serve to characterise the influences, and limitations, of idealised outer–inner interactions on global TBL dynamics, and highlight considerations for the design and optimisation of future flow control techniques.

**Key words:** boundary layer control, flow control, turbulent boundary layers

© The Author(s), 2026. Published by Cambridge University Press. This is an Open Access article, distributed under the terms of the Creative Commons Attribution licence (https://creativecommons.org/licenses/by/4.0/), which permits unrestricted re-use, distribution and reproduction, provided the original article is properly cited.



Downloaded from https://www.cambridge.org/core. University of Notre Dame, on 05 Oct 2026 at 13:53:55, subject to the Cambridge Core terms of use, available at https://www.cambridge.org/core/terms. https://doi.org/10.1017/jfm.2026.12085

Downloaded from https://www.cambridge.org/core. University of Notre Dame, on 05 Oct 2026 at 13:53:55, subject to the Cambridge Core terms of use, available at https://www.cambridge.org/core/terms. https://doi.org/10.1017/jfm.2026.12085



## 1. Introduction

Wall-bounded turbulent flows, such as the turbulent boundary layer (TBL), play an important role in governing the performance of a number of engineered systems. For instance, TBL dynamics is directly coupled with relevant system properties such as skin friction drag, aero-optical distortion, noise generation and heat transfer. Experiments conducted over many decades have also established that a hierarchy of quasi-periodic and repeating patterns of coherent motions, broadly referred to as structures, coexist within the TBL, as reviewed by Robinson (1991), and these structures are found to play a primary role in the production and maintenance of turbulence within the TBL. This stations the study of the dynamics/interactions of this hierarchy of structures coexisting within the TBL as fundamental to understanding global TBL dynamics which, in turn, is prerequisite to optimising strategies for their control and improving the performance of a wide range of engineered systems.

Specifically, the dynamics of large-scale structures (LSS), and their effect on relevant TBL properties, has been investigated extensively (Adrian *et al.* 2000; Ganapathisubramani *et al.* 2005; Guala *et al.* 2006; Adrian 2007; Hutchins & Marusic 2007*a*; Spencer *et al.* 2024). The term LSS is typically used to describe the organised groups, or packets, of coherent vortices that are formed in wall-bounded flows at sufficiently high friction Reynolds numbers ($Re_\tau > 2000$; Robinson 1991; Smits *et al.* 2011; Marusic & Monty 2019). Here, the term organised indicates that these coherent motions have characteristic length and time scales that can be measured. In the outer region of the TBL, the LSS can be identified by groups of spanwise-oriented vortices that form thin, inclined shear layers separating low- and high-speed regions of the flow, referred to as uniform momentum regions (Adrian *et al.* 2000; de Silva *et al.* 2016). In high Reynolds number TBLs, evidence of organised and energetic LSS can also be seen in the premultiplied one-dimensional (1-D) wavenumber energy spectra of the streamwise velocity fluctuations where a distinct peak emerges around the centre of the log-linear region ($y^+ = 3.9\,Re_\tau^{0.5}$; Klewicki *et al.* 2007; Mathis *et al.* 2009) and over a range of relatively long streamwise wavelengths centred around $\lambda_x \approx 4\delta - 6\delta$. In contrast, this outer peak is not present in the spectra of low Reynolds number TBLs ($Re_\tau < 2000$), which do not contain naturally occurring energetic LSS as described above (Hutchins & Marusic 2007*a*).

In addition, there is a relatively smaller-scale, organised and energetic structure located closer to the wall, whose characteristics are largely independent of the Reynolds number (Hutchins *et al.* 2009). This near-wall coherent structure is characterised by unsteady, small-scale, quasi-streamwise vortices ($\lambda_x^+ = 1000$), which give rise to characteristic streaks of low- and high-speed fluid between them ($\Delta z^+ = 100$), contained within the buffer region ($5 < y^+ < 30$; Kline *et al.* 1967; Robinson 1991). These near-wall vortices then create a significant spanwise variation in the streamwise velocity field (i.e. alternating low- and high-speed streaks), lending to their unsteadiness (Antonia & Bisset 1990). These unsteady near-wall vortices also lead to intermittent and quasi-cyclic events whereby low-speed fluid is ejected away from the wall, and high-speed fluid is transported towards the wall. These so-called burst–sweep events have been shown to be responsible for elevated levels of shear stress in the near-wall region, and for the significant production and maintenance of turbulence observed near the wall (Luchik & Tiederman 1987; Chen *et al.* 2021). As such, the characteristics of these streamwise vortices and streaks, along with the dynamics of the bursting events, are intimately related to flow properties such as skin friction drag (Kim 2011).

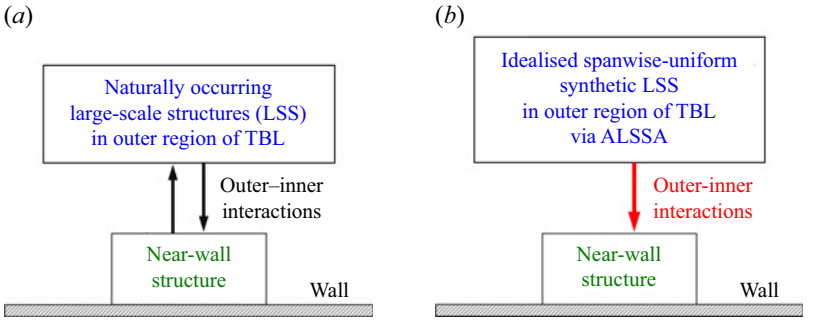



Figure 1. (*a*) Schematic of outer–inner interactions between small-scale turbulent structures near the wall and the naturally occurring LSS in the outer region of the TBL. (*b*) Schematic of the proposed approach to studying TBL interaction dynamics associated with idealised synthetic LSS.

Although several studies indicate that this near-wall turbulence production cycle is largely self-sustaining (Hamilton *et al.* 1995; Jiménez & Pinelli 1999; Panton 2001; Schoppa & Hussain 2002), it has also been found that the LSS can influence near-wall turbulence dynamics through some outer–inner interaction mechanism (Adrian *et al.* 2000). This is shown schematically in figure 1(*a*), whereby the distinct large- and small-scale structures of the TBL are coupled, to some extent, through outer–inner interactions (Robinson 1991; Guala *et al.* 2006). This conceptual model leads to two broad perceptions of global TBL structure. The first is a view in which the near-wall mechanism for coherent structure generation is largely autonomous of the outer LSS dynamics, as supported by previous studies of the near-wall region (Panton 2001; Schoppa & Hussain 2002; Thomas *et al.* 2019). The second is a view whereby increasingly energetic large-scale motions/structures in the outer region can significantly influence near-wall turbulence dynamics, the support for which is described in more detail in Hunt & Morrison (2000) and Corke & Thomas (2018). Underpinning this view, the dynamics of large- and small-scale motions within the log-linear and near-wall regions of the boundary layer have previously been shown, experimentally, to be correlated (Hutchins & Marusic 2007*b*; Mathis *et al.* 2011*a*). Further, utilising this observed correlation, a predictive model was developed in Mathis *et al.* (2011*a*) to estimate near-wall streamwise turbulence statistics based on large-scale motions measured only within the log-linear region. The success of this model suggested that there is a 'universal' near-wall region that is modified (or modulated) through inter-scale interactions with these large-scale motions (in the log-linear region and/or superimposed onto the near-wall region; Hutchins & Marusic 2007*b*; Mathis *et al.* 2011*a*; Andreolli *et al.* 2023). This so-called modulation phenomenon has also been measured experimentally (Mathis *et al.* 2009), and near the wall, there exists a distinct positive correlation between large-scale motions and the amplitude envelope of smaller-scale turbulent fluctuations. This correlation has also been found to extend to other regions of the TBL, other turbulent shear flows (Bandyopadhyay & Hussain 1984), and other flow properties such as the wall shear stress (Mathis *et al.* 2013). The strength of this correlation was also found to increase with the Reynolds number (Mathis *et al.* 2009), making these so-called classical amplitude modulating effects (which represent a specific subset of the nonlinear inter-scale interactions coexisting within the TBL; Lozier *et al.* 2024*a*) increasingly important in technologically relevant flows. Overall, these seemingly competing views of TBL dynamics suggest that a clearer characterisation of the mechanism(s) behind these inter-scale outer–inner interactions is needed, particularly for



Downloaded from https://www.cambridge.org/core. University of Notre Dame, on 05 Oct 2026 at 13:53:55, subject to the Cambridge Core terms of use, available at https://www.cambridge.org/core/terms. https://doi.org/10.1017/jfm.2026.12085

Downloaded from https://www.cambridge.org/core. University of Notre Dame, on 05 Oct 2026 at 13:53:55, subject to the Cambridge Core terms of use, available at https://www.cambridge.org/core/terms. https://doi.org/10.1017/jfm.2026.12085



the design and optimisation of flow control strategies (Chernyshenko *et al.* 2012; Corke & Thomas 2018; Andreolli *et al.* 2023).

To that end, active and passive flow control devices have also been used previously as tools to study TBL dynamics by selectively perturbing the TBL structures and studying the resulting flow response. Some of the earliest passive devices used to modify the LSS in the TBL were large-eddy-break-up (LEBU) devices (Corke *et al.* 1982; Dowling 1985; Savill & Mumford 1988; Kim *et al.* 2017; Chan *et al.* 2022). As reviewed by Alfredsson & Örlü (2018) and Corke & Thomas (2018), these devices were typically made from thin plates, aerofoils or rods elongated in the spanwise direction, and placed in the outer region of the boundary layer to disrupt naturally occurring large-scale motions and ultimately examine how near-wall dynamics were affected. Studies of these plate manipulators showed that they were effective (in certain conditions) at reducing near-wall turbulence intensity, reducing the frequency of bursting events, reducing local skin friction, and reducing streamwise boundary layer growth, among other effects (Corke *et al.* 1982; Dowling 1985; Savill & Mumford 1988; Kim *et al.* 2017; Chan *et al.* 2022). In Savill & Mumford (1988), it was shown that the interaction between the plate wake vortices and near-wall TBL structure was the primary mechanism for reducing skin friction drag; the maximum skin friction drag reduction always occurred close to the streamwise position where these wake vortices reached the sublayer.

Recently, the effect of active flow control devices that alter/induce large-scale motions/perturbations has also been studied (McKeon *et al.* 2018; Marusic *et al.* 2021; Meyers *et al.* 2025). For example, in a collection of experiments described in McKeon *et al.* (2018), a vertically oscillating element, referred to as a dynamic roughness element, was used to introduce a controlled travelling wave into the near-wall and log-linear regions of the TBL. Measurements of the synthetic modes highlight the periodic nature of these synthetic large-scale motions, introduced via the dynamic roughness element, which allowed for systematic study of their interactions with small-scale turbulence. Measurements of the correlation between these modes and smaller-scale turbulent motions showed that the synthetic large-scale motions had a strong effect/interaction with triadically coupled small-scale motions, and a phase-locking effect was observed in the near-wall structure of the TBL as a result (Duvvuri & McKeon 2015). Alternatively, motivated by intervention in the streak transient growth autonomous near-wall turbulence production mechanism proposed by Schoppa & Hussain (2002), pulsed-DC plasma actuation has also been used for active flow control, producing spanwise blowing confined to the buffer region of the TBL as described in Thomas *et al.* (2019). This approach has resulted in up to 78 % viscous drag reduction, and measurements of the mechanism for the observed drag reduction presented in Duong *et al.* (2021) and Meyers *et al.* (2025) were consistent with intervention in the streak transient growth mechanism. Scaling laws developed from this method were also verified in subsequent aerofoil experiments at free-stream Mach numbers up to $M_\infty = 0.5$ (as reported in Thomas *et al.* 2023), and a similar plasma actuation approach utilised by Cheng *et al.* (2021) to introduce near-wall streamwise vorticity also yielded significant viscous drag reduction in a flat plate TBL. Collectively, the results of these active flow control experiments demonstrate the significant effects that induced large-scale perturbations in the near-wall and log-linear regions can have on near-wall turbulence characteristics.

In Ranade *et al.* (2019), it was observed that large-scale perturbations imposed from outside the boundary layer could also modify near-wall turbulence characteristics. In this particular study, the TBL was 'forced' via the unsteady pressure field generated by a forced shear layer located well outside the boundary layer ($y \approx 4\delta$). The turbulence intensity inside the boundary layer was found to be both amplified and modulated by

Downloaded from https://www.cambridge.org/core. University of Notre Dame, on 05 Oct 2026 at 13:53:55, subject to the Cambridge Core terms of use, available at https://www.cambridge.org/core/terms. https://doi.org/10.1017/jfm.2026.12085



the this external forcing. This result demonstrates that, like the internal (near-wall) perturbations/forcings described above, large-scale perturbations to the outer region of the TBL can also affect the amplitude and organisation of structures within the rest of the TBL, and importantly in the near-wall region.

Inspired by these studies, an active flow control device in the form of a dielectric barrier discharge plasma-based actuator is used in the current study to introduce synthetic, periodic, spanwise-uniform, large-scale motions into the outer region of the TBL in order to investigate an idealised case of outer–inner layer interaction. It is important to note that the baseline TBL examined in this study had a Reynolds number that was purposely low enough that there were no naturally occurring energetic LSS in the outer region. Instead, the plasma actuator device was designed to introduce a well-controlled large-scale perturbation with variable streamwise wavelength (i.e. frequency) and amplitude, into the outer region of the boundary layer at a user-selected wall-normal location. This approach was tested previously, and the effect of this actuator device on the baseline canonical TBL was characterised parametrically, in Lozier *et al.* (2023, 2024*b*). These preliminary results confirmed that the actuator device could produce spanwise-uniform large-scale motions, with a range of user-selected wavelengths, and the introduction of these large-scale motions in the outer region resulted in modulation of the turbulence intensity (i.e. periodic changes in the magnitude of the turbulence intensity were observed) across the TBL, including the near-wall region, consistent with the other active flow control approaches described above. Further, the actuator design and methodology allowed for the generation of compact spanwise vortices, confined to the outer region, with streamwise wavelengths that fall within the characteristic range of large-scale motions, without introducing any direct/mechanical disruption to the near-wall region. However, it is important to note that specific characteristics of naturally occurring canonical LSS, such as their inherent three-dimensionality and stochastic spatial/temporal distribution (i.e. hairpin-like vortices, grouping/packets, meandering behaviours, etc.), are not replicated with the present actuator design, nor is it intended to do so. Instead, the synthetic perturbation produced here is well-suited to investigate an idealised case of outer–inner TBL interaction. An especially significant advantage to the present approach is that the imposed perturbation is periodic, which provides a convenient phase reference for separating the induced large-scale motions from the TBL's response to them. To that end, previous experimental (Lozier *et al.* 2024*b*) and numerical (Liu *et al.* 2022) studies have demonstrated that for a range of actuation frequencies and wall-normal forcing locations, significant modulation of the near-wall turbulence intensity can be achieved, phase-locked with the imposed perturbation in the outer region, and the observed modulation near the wall was found to be exclusively governed by the characteristics of the synthetic LSS confined to the outer region.

The present study aims to now investigate the process(es) by which these well-controlled and idealised large-scale motions imposed in the outer region of the TBL both superimpose onto, and modulate turbulence intensities within, the near-wall and log-linear regions of the TBL. This study further aims to investigate whether these imposed large-scale motions significantly influence the characteristics/dynamics of the near-wall turbulence generation cycle/structure.

## 2. Experimental set-up

The experiments presented in this study were performed in one of the low-turbulence, subsonic, in-draft wind tunnels located at the Hessert Laboratory for Aerospace Research at the University of Notre Dame. Experiments were performed in a test section of 0.6 m

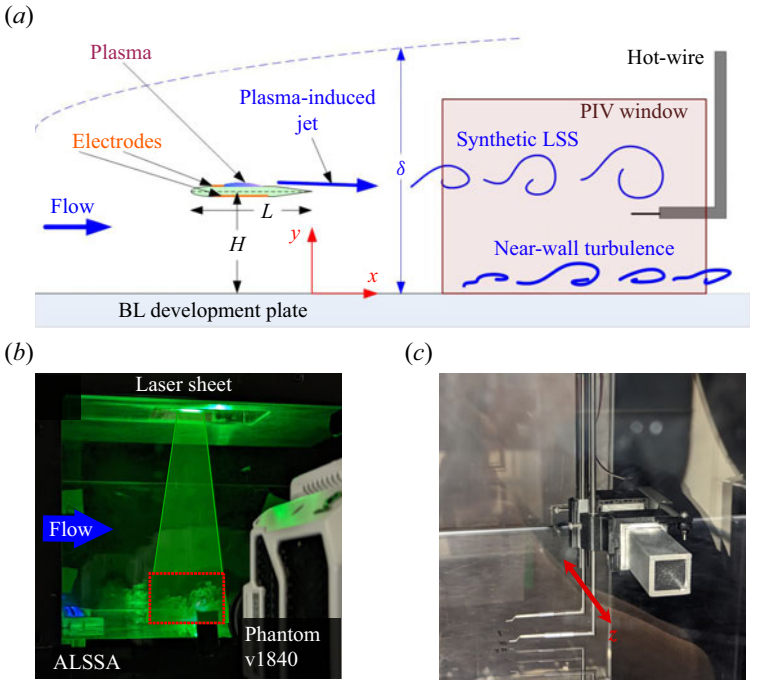



Figure 2. (*a*) Schematic of experimental set-up. (*b*) Photograph of particle image velocimetry set-up. (*c*) Photograph of spanwise offset hot-wire set-up.

square cross-section and 1.82 m length, with nominal free-stream turbulence levels of less than 0.1 %. The experimental set-up is shown schematically in figure 2(*a*). For this study, a flat, 2 m long, boundary layer development plate, which spanned the full test section width, was installed at the mid-height of the test section. The boundary layer development plate had a leading edge that was rounded into a semicircular profile with sandpaper distributed roughness attached in order to facilitate rapid turbulent transition on the top side.

A plasma-based active flow control actuator, as described below, was attached to the top side of the boundary layer development plate at a fixed streamwise location 140 cm downstream of the leading edge of the boundary layer development plate. This location was chosen to ensure both a long upstream TBL development length and a sufficient streamwise fetch for measurements before the end of the boundary layer development plate. The free-stream velocity was also measured to be constant between the actuator location and the end of the boundary layer development plate, confirming baseline zero-pressure gradient conditions throughout the measurement region.

A set of representative baseline TBL parameters were measured at $x = 3\delta$ downstream of the actuator trailing edge (150 cm downstream of the leading edge of the development plate) using a single hot-wire probe (additional details given in Lozier *et al.* 2024*b*). These parameters are summarised in table 1, for reference. The skin friction velocity $u_\tau$ and friction coefficient $c_f$ were determined using the Clauser method. The boundary layer thickness $\delta$ is taken as the classical 99 % thickness here. In all the experiments to be described in this study, the wind tunnel inlet free-stream velocity was set to $U_\infty = 7$ m s$^{-1}$ and was measured to be within $\pm 1$ % of the expected free-stream velocity before each measurement session.



Downloaded from https://www.cambridge.org/core. University of Notre Dame, on 05 Oct 2026 at 13:53:55, subject to the Cambridge Core terms of use, available at https://www.cambridge.org/core/terms. https://doi.org/10.1017/jfm.2026.12085

| $\delta$ | $\delta^*$ | $\theta$ | $U_\infty$ | $u_\tau$ | $c_f$ | $H_S$ | $Re_\theta$ | $Re_\tau$ |
|---|---|---|---|---|---|---|---|---|
| 34 mm | 5.3 mm | 3.9 mm | 7 m s$^{-1}$ | 0.31 m s$^{-1}$ | 0.0039 | 1.36 | 1770 | 690 |

Table 1. Representative canonical TBL parameters at $x = 3\delta$.

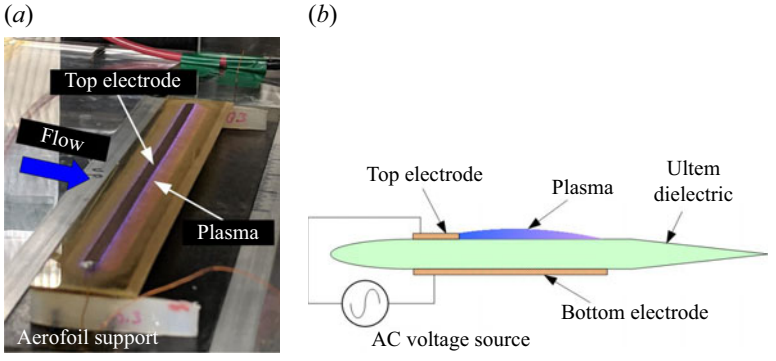



Figure 3. (*a*) Photograph of the ALSSA. (*b*) Schematic of an alternating current dielectric barrier discharge plasma actuator showing essential components (electrode thicknesses are exaggerated for clarity).

As shown in figure 3, the plasma-based active large-scale structure actuator (ALSSA) was used in this study to introduce periodic, spanwise-uniform plasma-induced forcing into the outer region of the TBL. The actuator plate was made from a 2 mm thick sheet of Ultem, a dielectric polymer. The dimensions of the actuator plate were $W = 25$ cm ($W = 8\delta$, $W^+ = 5600$) width in the spanwise direction, and $L = 32$ mm ($L \approx 1\delta$, $L^+ = 640$) length in the streamwise direction. This actuator width is sufficient to conservatively ensure that an approximately $5\delta$ wide region of spanwise-uniform flow is maintained across all downstream measurement locations, despite the three-dimensional end effects from the finite-length actuator plate, as demonstrated in Lozier *et al.* (2024*b*). The streamwise extent and thickness of the actuator plate were minimised, within safe margins for plasma generation, the leading edge of the dielectric plate was rounded, and the last 10 mm of the trailing edge were linearly tapered to half-angle 10° to minimise the wake downstream of the actuator plate. The plasma actuator was supported above the boundary layer development plate by twin NACA0010 aerofoils that were fabricated at user-selected heights such that the distance between the actuator plate and wall was fixed at $H = 0.3\delta$ ($H^+ = 200$) for these experiments. This wall-normal position of the ALSSA device was found to induce the strongest response of the TBL in the near-wall region and was deemed optimal for the aims of the current study. Additional details about the optimisation of the ALSSA device can be found in Lozier *et al.* (2024*b*).

Electrodes were attached to the dielectric plate in order to generate a spanwise-uniform plasma jet on the top side of the actuator, as shown schematically in figure 3(*b*). An upper surface electrode of 0.05 mm thick copper foil tape was placed 15 mm from the dielectric plate leading edge, and was 4 mm in length (streamwise), and 22 cm in width (spanwise). On the bottom surface, a second copper foil electrode was aligned with the top electrode but was 12 mm in length. Additional details regarding the construction and operation of the actuator can be found in Lozier (2023).



Downloaded from https://www.cambridge.org/core. University of Notre Dame, on 05 Oct 2026 at 13:53:55, subject to the Cambridge Core terms of use, available at https://www.cambridge.org/core/terms. https://doi.org/10.1017/jfm.2026.12085

Alternating current dielectric barrier discharge plasma was produced by connecting the copper electrodes on the top and bottom of the actuator to a high voltage AC source (Thomas *et al.* 2009), as shown in figure 3(*b*), which provided a 40 kV peak-to-peak sinusoidal waveform excitation to the electrodes at a frequency of 4 kHz. The peak-to-peak voltage from the high-voltage AC system was measured during experiments and maintained within $\pm 5\,\%$ of the expected excitation voltage. As shown schematically in figure 2(*a*), a plasma jet was formed above the top surface of the actuator plate above the exposed portion of the lower surface electrode. At the 4 kHz actuation carrier frequency, the plasma actuator operates in a quasi-steady mode, essentially creating a spanwise-uniform, steady, plasma-induced jet above the actuator plate directed in the streamwise direction (Thomas *et al.* 2009). To introduce the desired periodic forcing, the sinusoidal waveform used to generate the plasma jet was modulated by a square wave with a 50 % duty cycle oscillating at the desired forcing frequency. In the experiments presented here, the forcing frequency was fixed at $f_P = 80$ Hz ($f_P\delta/U_\infty = 0.39$), which was again found to create the strongest response of the TBL within the near-wall region, which is optimal for this study. A detailed discussion for this choice is provided in Lozier *et al.* (2024*b*).

Because the physical presence of the actuator plate alone may alter characteristics of the canonical TBL, three measurements of the boundary layer were taken to systematically analyse the effect of the plasma actuation. The first measurement was of the canonical TBL (no actuator plate), which served as a baseline. Next, measurements were taken with the actuator plate installed, but no active plasma forcing, which will be referred to as the 'plate-only' case. Finally, measurements were taken with active plasma forcing, under the conditions described above, which will be referred to as the 'plasma-on' case.

### 2.1. *Particle image velocimetry*

In all particle image velocimetry (PIV) experiments reported here, a double-pulsed 532 nm laser (EverGreen 200 laser with 200 mJ pulse and 10 ns pulse width) was used to make phase-locked, spatially resolved, planar flow field measurements. The flow was seeded with DEHS particles (diameter $< 1\,\mu$m) through the tunnel inlet, which were illuminated in the streamwise wall-normal plane. Diverging laser sheets (half-angle 10°) were formed and directed through the top of the test section and down onto the boundary layer development plate, resulting in spanwise thickness <2 mm at the boundary layer development plate; see figure 2(*b*). The overlap of these laser sheets resulted in a maximum measurement region of $x = 60 \times y = 24$ mm ($x = 1.8 \times y = 0.7\delta$). Seven measurement regions along the same wall-normal/streamwise plane were used with a minimum overlap of 10 % ($\Delta x_{overlap} \geqslant 0.2\delta$) between neighbouring regions, resulting in a total experimental streamwise measurement region approximately $x = 0.2\delta - 10\delta$ downstream of the actuator (with the leading edges of these regions located at approximately $x/\delta = -0.1$, 1.1, 2.5, 4.0, 5.5, 6.8 and 8). The closest reliable measurement point to the actuator was limited to $x \approx 0.2\delta$ downstream of the trailing edge of the actuator due to optical constraints of the experimental set-up.

The separation between consecutive laser pulses was $\Delta t = 50\,\mu$s, and laser pulses were created with repetition frequency 12.5 Hz, phase-locked with the plasma forcing cycle. Images were captured with a Phantom v1840 high-speed camera at sampling frequency 100 Hz (phase-locked with both laser pulses and plasma forcing cycle) with resolution $1920 \times 1080\,\text{px}^2$. This resulted in a final measurement resolution of $12\,\Delta x^+ \times 12\,\Delta y^+$. Additional details of the camera, lens and processing parameters used in these experiments can be found in Lozier (2023). The error of the computed velocity vectors was estimated to be $\epsilon_u/U_\infty < 0.5\,\%$ ($\epsilon_u < 0.1u_\tau$). As mentioned above, the PIV image acquisition and



Downloaded from https://www.cambridge.org/core. University of Notre Dame, on 05 Oct 2026 at 13:53:55, subject to the Cambridge Core terms of use, available at https://www.cambridge.org/core/terms. https://doi.org/10.1017/jfm.2026.12085

plasma forcing cycles were phase-locked, and due to the specific frequency chosen for the laser pulse repetition, there were five distinct phases of the plasma forcing cycle ($\phi = 0, 2\pi/5, 4\pi/5, 6\pi/5, 8\pi/5$ radians) measured non-sequentially over the course of 32 actuation periods. Over the total sampling time $T_s = 480$ s, each phase of the plasma forcing cycle was measured $n = 1200$ times, to obtain reasonable convergence of the phase-locked statistics. This PIV configuration resulted in measurements of the two-dimensional velocity field that were phase-locked, spatially resolved in the streamwise and wall-normal directions, and measured over a long streamwise extent downstream of the actuator.

### 2.2. *Hot-wire anemometry*

To measure spanwise spatial correlations of the streamwise velocity, a constant-temperature anemometer with two boundary-layer-style hot-wire probes (Dantec 55P15) with diameters 5 µm and lengths $l = 1.5$ mm ($l^+ = 30$) were used to collect time series of the streamwise component of velocity across a range of spanwise separations; see figure 2(*c*). The sampling frequency was $f_S = 30$ kHz, with a low-pass filter set to 10 kHz, and the sampling time was $T_S = 90$ s for each case, such that $t^+ = u_\tau^2/(f_S\nu) \approx 0.2$ and $T_S U_\infty/\delta \approx 19\,000$. The first hot-wire was held stationary at the mid-span of the test section (which also corresponds to the mid-span of the actuator). The second hot-wire, mounted on a spanwise-oriented traversing stage, was attached to the stationary hot-wire and matched in $x$ and $y$ positions. Measurements were taken simultaneously, with the hot-wires starting at minimum separation $\Delta z = 2$ mm ($\Delta z^+ = 40$), and reaching maximum separation approximately $\Delta z = 1.1\delta$ ($\Delta z^+ = 760$). For all of the results presented here, the probes were positioned at the farthest downstream location achievable, $x = 8\delta$, as measured downstream of the plasma actuator's trailing edge.

## 3. Data reduction

Phase-locked analysis was performed independently at each $(x, y, z)$ location, for both the PIV and hot-wire measurements. Since the actuator introduces periodic forcing into the flow, it is both convenient and necessary to phase-lock measurements to the periodic forcing frequency in order to separate the induced large-scale motions from the response of the TBL (across a broad hierarchy of scales; Ranade *et al.* 2019). To implement phase-locked analysis, a triple Reynolds decomposition of the streamwise velocity was utilised:

$$u(y, t) = U(y) + \tilde{u}(y, \phi) + u'(y, \phi, n), \tag{3.1}$$

where $u$ is the instantaneous streamwise velocity, $U$ is the time mean component of velocity, $\tilde{u}$ is a phase-dependent or modal velocity component, $u'$ is a velocity fluctuation, and $\phi$ is the phase of the plasma actuation cycle. Here, $\phi$ can be defined by

$$\phi = \left(\frac{t_n}{T_P} - n\right) 2\pi, \tag{3.2}$$

where $n$ represents an actuator period ($T_p = 1/f_p$) length sample, or realisation, of the original velocity time series. These $n$ realisations are extracted from the full time series such that the beginning of each realisation is aligned with the plasma being turned on in the actuation cycle. In (3.2), $t_n$ is a time in the $n$th realisation, which is related to the phase angle $\phi$ by the period of the actuation cycle. Then $n$ realisations of the mean removed velocity can be ensemble averaged to find the modal component of velocity as a function



Downloaded from https://www.cambridge.org/core. University of Notre Dame, on 05 Oct 2026 at 13:53:55, subject to the Cambridge Core terms of use, available at https://www.cambridge.org/core/terms. https://doi.org/10.1017/jfm.2026.12085

of the phase angle:

$$\tilde{u}(y, \phi) = \langle u(y, \phi, n) - U(y) \rangle_n. \tag{3.3}$$

Here, the angle brackets denote ensemble averaging over all realisations. This modal velocity will be used to quantify the periodic, large-scale perturbation/motions induced by the actuator. The velocity fluctuations $u'$ that remain after removing both the modal and mean components of velocity from each realisation were then used to compute an ensemble-averaged root mean square (RMS):

$$u'_{RMS}(y, \phi) = \sqrt{\langle u'(y, \phi, n)^2 \rangle_n}. \tag{3.4}$$

We will refer to this quantity as the residual turbulence amplitude. The phase-averaged mean was also removed from the residual turbulence amplitude to define a phase-dependent change in the residual turbulence amplitude,

$$\Delta u'_{RMS}(y, \phi) = u'_{RMS}(y, \phi) - \left\langle u'_{RMS}(y, \phi) \right\rangle_\phi. \tag{3.5}$$

This new quantity is especially useful because it reveals changes in the distribution of velocity fluctuations that are phase-locked with the plasma actuation cycle. Further, removing the phase-averaged mean from the residual turbulence amplitude makes it easy to compare relative changes in the turbulence intensity across all wall-normal locations. As such, this new quantity (3.5), referred to concisely as the residual turbulence, will be used to quantify the TBL's response to the periodic perturbation induced by the actuator. The phase-locking treatments presented thus far will also be applied to other flow field quantities, such as the wall-normal velocity and Reynolds stress, in later analysis; (3.3) and (3.4) can be used to analyse any quantity of interest, but have been shown with the streamwise component of velocity here for reference.

It should be noted here that velocity fluctuations can alternatively be decomposed using methods such as scale-based (or frequency-based) filtering (McKeon *et al.* 2018), to separate the motions that are induced by the plasma forcing from the smaller-scale turbulent motions of the TBL. While employing a frequency-based filtering method is not feasible for the present PIV data (insufficient temporal resolution), this method was tested extensively with the hot-wire data from previous experiments. The results from frequency-based filtering and the phase-locked analysis presented here were compared, and identical behaviours/results were observed for all streamwise and wall-normal locations, except for those in the immediate vicinity of the actuator plate (Lozier 2023). The discrepancies in the immediate vicinity of the actuator plate likely stem from the small-scale turbulence that is directly introduced by the actuator plate's wake. However, the results presented in the next section are primarily focused on the region between the actuator plate and the wall. Additionally, the residual turbulence amplitude was found to contain a relatively small contribution from cycle-to-cycle variability in the synthetic LSS, in addition to the primary contribution from smaller-scale turbulent motions. However, this contribution is not phase-dependent, therefore it is removed from the residual turbulence in (3.5). As such, the modal velocity and residual turbulence that are obtained from this phase-locked analysis of the PIV (and hot-wire) data are expected to be (approximately) equivalent to the results that would be obtained from a frequency-based filtering method. Further, this agreement supports the interpretation that the new residual turbulence quantity is representative of the TBL's response (specifically from small-scale turbulent motions) to the periodic perturbation induced by the actuator.



Downloaded from https://www.cambridge.org/core. University of Notre Dame, on 05 Oct 2026 at 13:53:55, subject to the Cambridge Core terms of use, available at https://www.cambridge.org/core/terms. https://doi.org/10.1017/jfm.2026.12085

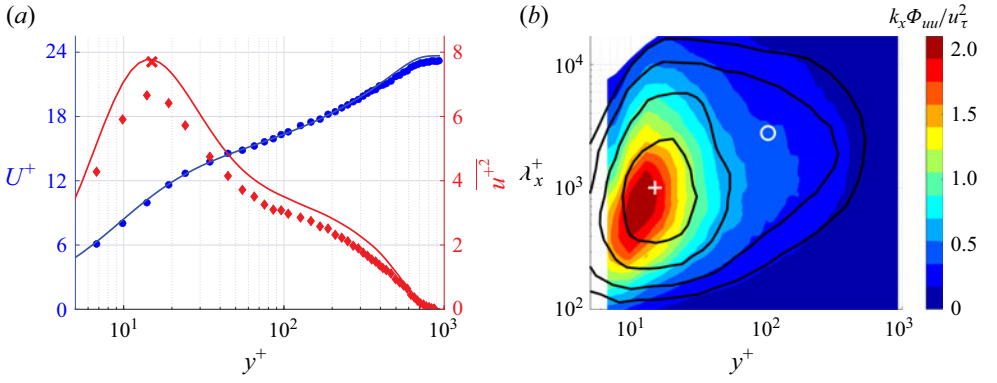



Figure 4. (*a*) Streamwise mean velocity and turbulence intensity for the baseline canonical TBL (Lozier *et al.* 2024*b*). Solid lines are $Re_\tau = 690$ DNS data from Jiménez *et al.* (2010). The red '×' is the peak turbulence intensity corrected for hot-wire spatial filtering effects (Hutchins *et al.* 2009). (*b*) Premultiplied 1-D wavenumber energy spectra (Lozier *et al.* 2024*b*). The plus marks the inner peak ($y^+ = 15$, $\lambda_x^+ = 1000$), and the open circle marks the theoretical outer-peak location ($y^+ = 3.9\,Re_\tau^{0.5}$, $\lambda_x^+ \approx 2700$). Contour lines are $Re_\tau = 1100$ experimental data from Hutchins & Marusic (2007*b*). Here, $x = 3\delta$.

## 4. Results

The baseline canonical TBL for this experiment was quantified using a single hot-wire probe in Lozier *et al.* (2024*b*), and statistical and spectral representations of this baseline TBL are shown in figure 4, for reference.

The inner-variable scaled streamwise mean velocity and turbulence intensity profiles in figure 4(*a*) match the direct numerical simulation (DNS) results from Jiménez *et al.* (2010) at a comparable friction Reynolds number when the effect of the finite hot-wire length is accounted for (note the red '×') as recommended by Hutchins *et al.* (2009). The extent of the log-linear region for the baseline TBL was determined to be within $50 < y^+ < 200$, and the mean geometric location was determined to be at $y^+ = 100$, which is very close to the expected value $y^+ = 3.9\,Re_\tau^{0.5}$ (Klewicki *et al.* 2007; Mathis *et al.* 2009). Similarly, the premultiplied 1-D wavenumber energy spectra in figure 4(*b*) agree well with experimental data from Hutchins & Marusic (2007*b*) with a similar Reynolds number. Most important in figure 4(*b*) is the lack of a naturally occurring outer LSS energy peak for the baseline TBL, as desired for this study.

A statistical description of the effects of the ALSSA device on this baseline canonical TBL, from single-point hot-wire measurements, has been given in Lozier *et al.* (2024*b*). The streamwise mean velocity and turbulence intensity from Lozier *et al.* (2024*b*) for the canonical, plate-only and plasma-on cases are re-plotted here in figure 5. When the actuator plate is added to the baseline TBL, with no active forcing, there is a decrease in both the mean velocity and turbulence intensity around the actuator plate location (vertical dashed line in figure 5), consistent with a low momentum deficit wake being induced by the actuator plate (also consistent with previous studies of LEBU devices; Corke *et al.* 1982; Chan *et al.* 2022). When active plasma forcing is added, there is some recovery in both the streamwise mean velocity and turbulence intensity, towards the canonical levels, especially above the plate location ($y^+ = 200$) where the plasma jet is located ($y^+ \approx 265$). It is also noted that near the wall ($y^+ < 40$), there is no effect of the plasma forcing on the (time-averaged) turbulence intensity, as compared to the plate-only case, at this streamwise location; however, in previous studies, an increase in the peak plasma-on turbulence intensity was observed farther downstream (e.g. at $x = 8\delta$, where an increase



Downloaded from https://www.cambridge.org/core. University of Notre Dame, on 05 Oct 2026 at 13:53:55, subject to the Cambridge Core terms of use, available at https://www.cambridge.org/core/terms. https://doi.org/10.1017/jfm.2026.12085

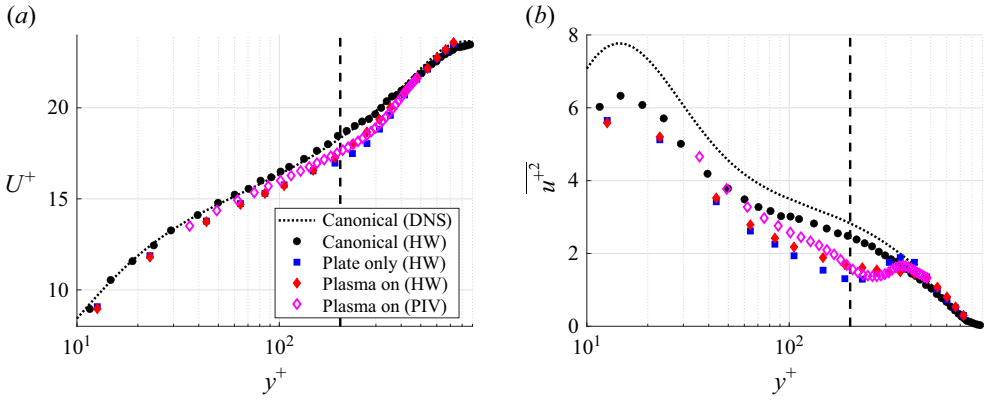



Figure 5. Comparison of canonical, plate-only and plasma-on statistics measured using hot-wire (HW) and PIV: (*a*) streamwise mean velocity and (*b*) turbulence intensity. Hot-wire data are from Lozier *et al.* (2024*b*). Matched $Re_\tau$ DNS are from Jiménez *et al.* (2010). The vertical dashed line represents the location of the actuator plate. Here, $H^+ = 200$, $f_p = 80$ Hz, $x = 5\delta$.

was also observed for the time-averaged Reynolds stress and turbulence production; Lozier 2023).

Next, results from the planar PIV measurements of the region downstream of the actuator will be presented to both complement and expand upon these earlier results. These new PIV measurements are unique from the previous measurements in a few key ways. First, they are spatially resolved in the streamwise direction, over a large streamwise extent, meaning that the true spatially evolving response of the TBL can be discerned. They also remain phase-resolved, although at a much lower resolution than previous measurements. And finally, direct measurement of the wall-normal component of the velocity (in addition to the streamwise component), over a spatially resolved two-dimensional field allows for direct calculation of new flow properties such as the Reynolds shear stress and vorticity.

Statistical profiles from the plasma-on case, measured using the planar PIV system, are validated here by comparison with the results from Lozier *et al.* (2024*b*) in figure 5. The streamwise mean velocity at a single downstream location is shown in figure 5(*a*), and there is good agreement between the plasma-on profile measured using PIV and the earlier measurement using a single hot-wire. Similarly, there is good agreement in the streamwise turbulence intensity profile measured using PIV in figure 5(*b*). The streamwise turbulence intensity measured using PIV appears to be consistently higher in magnitude than the hot-wire result, which can be attributed to the relatively finer spatial resolution of the planar PIV and/or higher measurement noise.

To identify the locations of ALSSA-induced vortical structures, the $\lambda_2$-criterion defined by Jeong & Hussain (1995) was used:

$$\lambda_2 = \frac{\partial \tilde{u}^2}{\partial x} + \frac{\partial \tilde{v}}{\partial x}\frac{\partial \tilde{u}}{\partial y}. \tag{4.1}$$

These results are presented in figure 6(*a*). The map of $\lambda_2$ has been normalised by the maximum absolute value (called $\lambda_0$) such that a value $\lambda_2/\lambda_0 = -1$ would indicate a clockwise rotating spanwise vortical structure in the flow. From this map of $\lambda_2$, it is now possible to identify the instantaneous locations of the synthetic LSS in the outer region. The approximate locations of synthetic spanwise vortices are indicated with yellow circles in figure 6(*a*) (corresponding to regions $\lambda_2/\lambda_0 \approx -1$), which indicate streamwise



Downloaded from https://www.cambridge.org/core. University of Notre Dame, on 05 Oct 2026 at 13:53:55, subject to the Cambridge Core terms of use, available at https://www.cambridge.org/core/terms. https://doi.org/10.1017/jfm.2026.12085

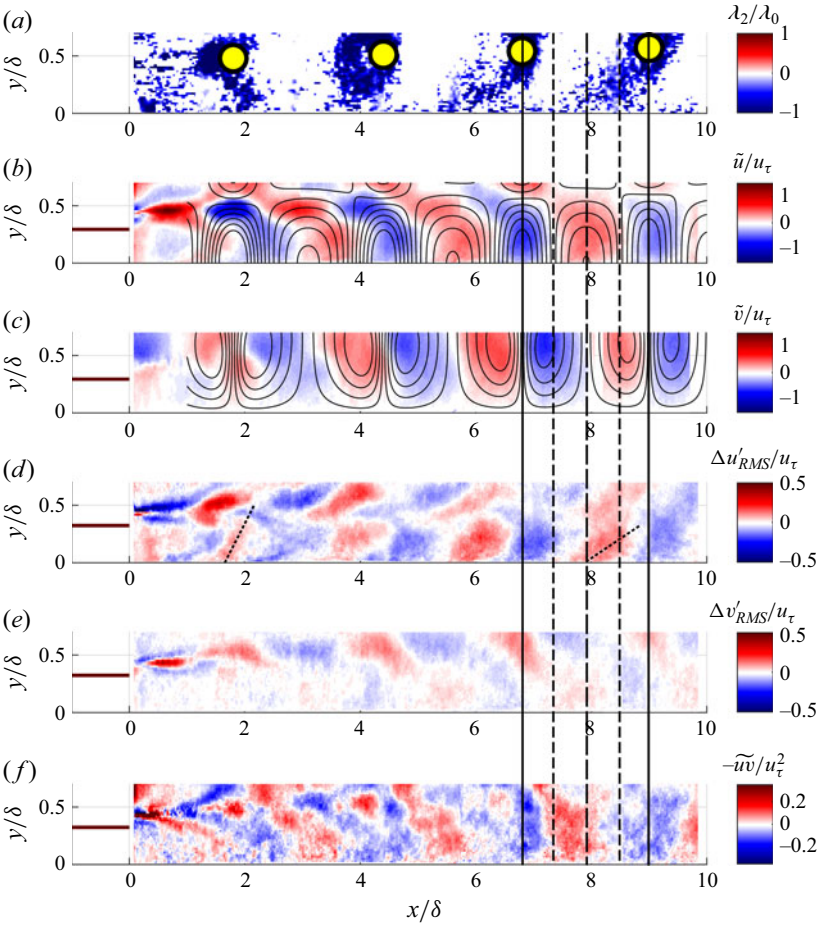



Figure 6. (*a*) Plot of $\lambda_2$ from (4.1). (*b*) Streamwise component of modal velocity. (*c*) Wall-normal component of modal velocity. (*d*) Streamwise component of residual turbulence. (*e*) Wall-normal component of residual turbulence. (*f*) Phase-averaged Reynolds stress. Here, $H = 0.3\delta$, $f_p = 80$ Hz.

wavelength approximately $\lambda_x = 2\delta$ for the synthetic LSS. A single phase of the actuation cycle is shown in figure 6, which corresponds to the plasma being turned on ($\phi = 0$).

Spatially resolved maps of the streamwise and wall-normal components of modal velocity obtained via planar PIV are also presented in figures 6(*b*) and 6(*c*). Here, the physical location and dimension of the actuator plate are shown by the dark horizontal bar on the left-hand side of each map. Above the actuator, there are distinct and periodic fluctuations in the streamwise modal velocity associated with the plasma jet that is generated on the top side of the actuator (figure 6*b*). There are also fluctuations, of comparable magnitude to the friction velocity, in the region between the actuator and the wall, with the highest amplitude primarily around the log-linear region (nominally $y^+ = 100$, $y/\delta = 0.15$), that occur slightly downstream of the same-signed fluctuations above the actuator. The induced variations in the streamwise modal velocity below the actuator also extend nearly to the wall, though the amplitude of the variations begins to diminish significantly as the wall is approached. Similarly, there are fluctuations in the wall-normal modal velocity, also comparable in magnitude to the friction velocity,



Downloaded from https://www.cambridge.org/core. University of Notre Dame, on 05 Oct 2026 at 13:53:55, subject to the Cambridge Core terms of use, available at https://www.cambridge.org/core/terms. https://doi.org/10.1017/jfm.2026.12085

Downloaded from https://www.cambridge.org/core. University of Notre Dame, on 05 Oct 2026 at 13:53:55, subject to the Cambridge Core terms of use, available at https://www.cambridge.org/core/terms. https://doi.org/10.1017/jfm.2026.12085



across the entire wall-normal measurement extent (figure 6*c*). However, for the wall-normal modal velocity, the fluctuations above and below the actuator location are in phase, especially at the most downstream locations. These results are indicative of the distinct spanwise vortices induced by the plasma forcing and consistent with previous experimental single point hot-wire measurements (Lozier *et al.* 2023) and results for a numerically simulated actuated boundary layer (Liu *et al.* 2002).

These streamwise and wall-normal modal velocity fields were also modelled using Biot–Savart induction considering point vortex sources (and their corresponding images) which are representative of these synthetic LSS (i.e. the yellow circles in figure 6*a*). Contours of the velocity fields generated from the Biot–Savart induction model are overlaid in figures 6(*b*) and 6(*c*), with contour levels $-1.5 : 0.3 : 1.5$. With proper adjustment of the circulation and diffusion for each point vortex, the reconstructed modal velocities match in not only their spatial distribution, but also amplitude starting from approximately $x = 4\delta$. The fluctuations in modal velocity closer to the actuator are not as well explained through this Biot–Savart model, as the induced velocity fluctuations immediately downstream of the actuator trailing edge, $x = 0{-}2\delta$, may be influenced by secondary effects due to the local flow conditions (i.e. induced pressure gradients and/or circulation) around the actuator plate during plasma forcing. However, the agreement of the measured phase-locked velocities with this Biot–Savart model and the spatial input–output model of Liu *et al.* (2022) demonstrates that the superimposition of significant large-scale motions from the outer region onto the log-linear and near-wall regions can be modelled through simple linear processes.

It is also noteworthy that the streamwise and wall-normal modal velocity measured in this experiment, figures 6(*b*) and 6(*c*), are similar in both amplitude and spatial distribution to the same quantities measured in experiments where large-scale motions were introduced via dynamic wall roughness (Huynh & McKeon 2020). The similarity in results demonstrates that the actuator design used here can achieve effective large-scale modification of the near-wall velocity without being physically located at, or near, the wall. Additionally, the streamwise modal velocities measured using the spanwise offset hot-wires at two representative wall-normal locations near the downstream end of the PIV domain are shown in figures 7(*a*) and 7(*b*). Over separation distances $\Delta z$ of up to one boundary layer thickness, the streamwise modal velocities measured in the near-wall and log-linear regions are identical (in amplitude and phase, within experimental uncertainty) to the measurement at the mid-span (which also agrees well with the mid-span PIV measurement). This confirms the extent of spanwise-uniform flow that is induced by the actuator, and indicates that the results from figure 6 are representative of the flow over a significant spanwise distance, not just the mid-span.

In addition to the modal velocity, the components of residual turbulence are presented in figures 6(*d,e*). In the streamwise residual turbulence (figure 6*d*), there is a visual distinction between fluctuations around the actuator height (a signature of the synthetic LSS themselves), and fluctuations in the near-wall region (the TBL response, i.e. modulated turbulence intensity). This is especially clear just downstream of the actuator, $x = 4\delta$, where two spatially distinct regions of positive residual turbulence fluctuation can be seen. Above the actuator height, $y/\delta = 0.5$, the residual turbulence fluctuations associated with the synthetic LSS decay in the downstream direction. In contrast, the residual turbulence fluctuations below the actuator, which represent the TBL response to the imposed LSS, are growing in amplitude until approximately $x = 7\delta$ downstream of the actuator, where they also begin to decay. The maximum amplitude of residual turbulence below the actuator, across all streamwise locations, is consistently around the log-linear region of the TBL, $y^+ \approx 100$, $y/\delta \approx 0.15$, and of the order of the friction velocity. This distinct region of

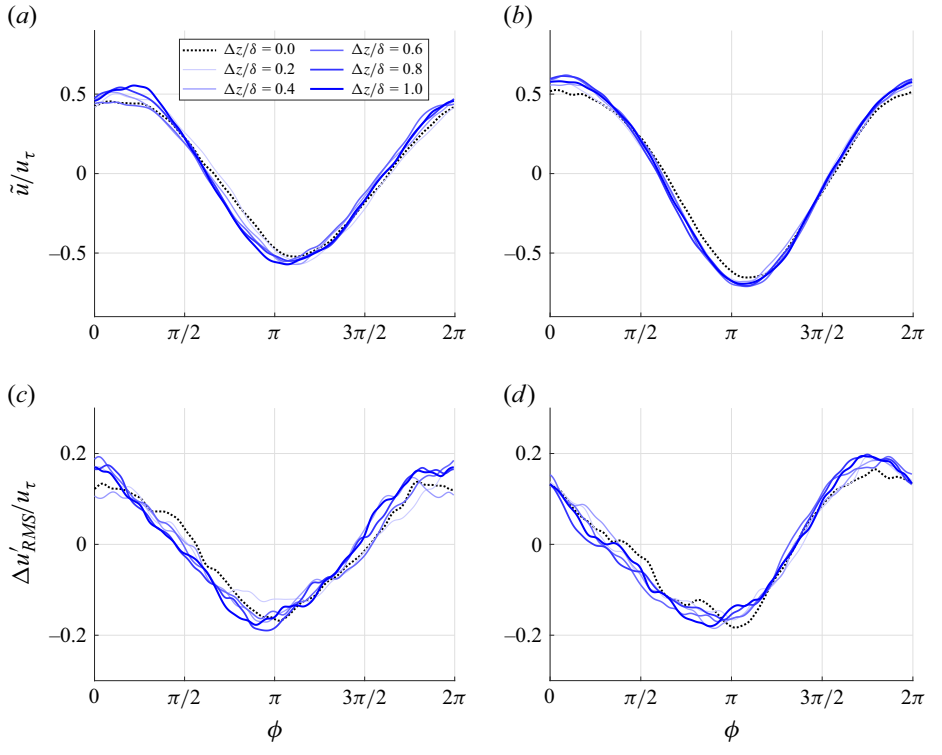



Figure 7. Phase-dependent variations in (*a*,*b*) modal velocity and (*c*,*d*) residual turbulence at (*a*,*c*) $y^+ = 25$ and (*b*,*d*) $y^+ = 100$ across multiple spanwise locations. Here, $H^+ = 200$, $x = 8\delta$, $f_P = 80$ Hz.

modulated turbulence also changes shape, or orientation, moving downstream, as shown by the dashed lines in figure 6(*d*), which correspond to inclinations from the wall of 45° (left) and 20° (right). In previous experiments, it was determined that the inclination of this region of modulated turbulence was similar to the typical inclination of attached eddies, which can vary across the TBL over 15°−45° (Adrian *et al.* 2000), which is now confirmed here with spatially resolved measurements. This shape is also similar to, and aligns with, the vorticity pattern extending to the wall as shown in figure 6(*a*). At the farthest downstream locations, starting at approximately $x = 8\delta$, the two previously distinct regions of residual turbulence fluctuations begin to blend or interact. These behaviours demonstrate an evolution or adjustment of the TBL from its canonical state in response to the presence of the synthetic LSS. Similar to the conclusions about the modal velocity, fluctuations in the residual turbulence near the wall immediately downstream of the actuator should not be attributed directly to the synthetic LSS, which are not yet well-defined (i.e. not fully developed).

The streamwise component of the residual turbulence was also measured using the spanwise offset hot-wires as shown in figures 7(*c*) and 7(*d*). Over separation distances of up to one boundary layer thickness, the streamwise residual turbulence also remains identical to the measurement at the mid-span of the tunnel. This again confirms the significant extent of spanwise-uniform flow that is produced by the actuator, and shows that the TBL response is also spanwise uniform across this extent.

For the wall-normal component of the residual turbulence, shown in figure 6(*e*), significant fluctuations are only observed in the region above the actuator. Further, these



Downloaded from https://www.cambridge.org/core. University of Notre Dame, on 05 Oct 2026 at 13:53:55, subject to the Cambridge Core terms of use, available at https://www.cambridge.org/core/terms. https://doi.org/10.1017/jfm.2026.12085

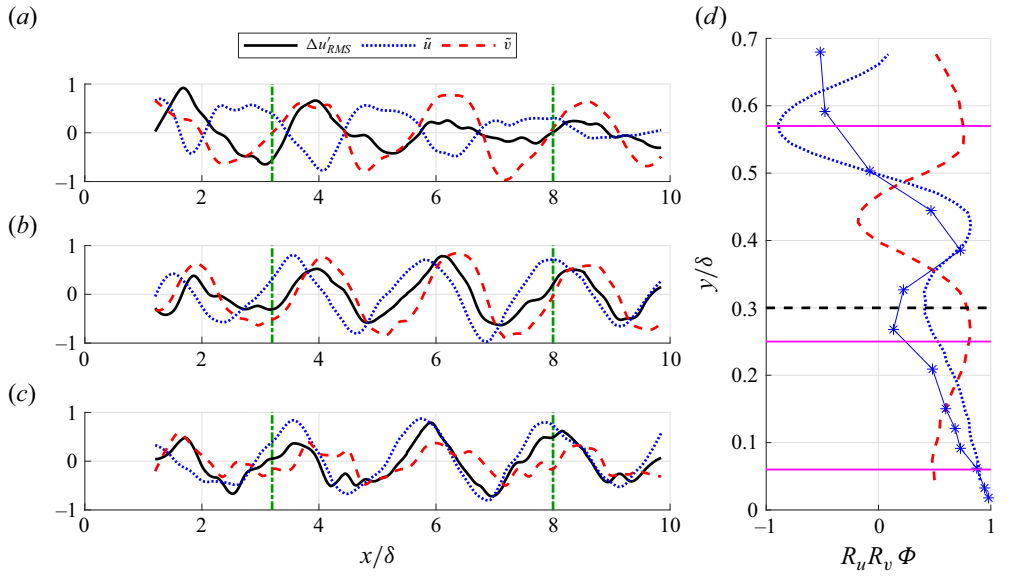



Figure 8. Normalised traces of streamwise modal velocity, wall-normal modal velocity and streamwise residual turbulence at (*a*) $y/\delta = 0.57$ ($y^+ = 400$), (*b*) $y/\delta = 0.24$ ($y^+ = 160$) and (*c*) $y/\delta = 0.06$ ($y^+ = 40$). (*d*) Normalised correlation between residual turbulence and modal velocities ($R_u$ indicated by the blue dotted line, $R_v$ indicated by the red dashed line). Vertical green dash-dotted lines in (*a*,*b*,*c*) indicate approximate bounds for correlation region. Blue asterisks are $\Phi$ modulation coefficients from Lozier *et al.* (2024*b*). Solid magenta lines correspond to locations of traces in (*a–c*). Actuator location marked by horizontal dashed line. Here, $H = 0.3\delta$, $f_p = 80$ Hz.

fluctuations are of the same magnitude as the streamwise component in this region, and therefore also considered a direct signature of the synthetic LSS themselves. Critically, the absence of similar fluctuation signatures below the plate confirms that these synthetic vortical structures remain confined to the outer region, and do not physically encroach into the near-wall or log-linear regions. This also indicates that the modulation of the streamwise residual turbulence observed below the actuator plate in figure 6(*d*) is not an artefact of the synthetic LSS themselves, but induced through some outer–inner interaction. The map of the phase-dependent Reynolds stress is shown in figure 6(*f*). There are fluctuations in the Reynolds stress across the entire measurement region, and the fluctuations have a nearly constant amplitude across spatial locations. It is noted that in the log-linear and near-wall regions, positive peaks in $-\widetilde{uv}/u_\tau^2$ lead peaks in residual turbulence, and by the downstream location $x = 7\delta$, the fluctuations have become somewhat organised in the wall-normal direction, with a shape similar to the wall-normal modal velocity. It is also noted that the above PIV measurements, of all turbulence quantities, are consistent with the results presented in previous studies for single-point hot-wires (Lozier *et al.* 2024*b*).

To further investigate the relationship between fluctuations in the streamwise residual turbulence and both components of modal velocity, streamwise traces of each quantity have been extracted at three representative wall-normal locations in figures 8(*a–c*). The normalised spatial correlations between each component of the modal velocity ($\tilde{u}$, $\tilde{v}$) and the change in residual turbulence ($\Delta u'_{RMS}$) across all wall-normal locations,



Downloaded from https://www.cambridge.org/core. University of Notre Dame, on 05 Oct 2026 at 13:53:55, subject to the Cambridge Core terms of use, available at https://www.cambridge.org/core/terms. https://doi.org/10.1017/jfm.2026.12085

$$R_{u_i}(y) = \frac{\left\langle \tilde{u_i}(x, y, \phi)\, \Delta u'_{RMS}(x, y, \phi) \right\rangle_x}{\sqrt{\langle \tilde{u_i}(x, y, \phi)^2 \rangle_x}\, \sqrt{\left\langle \Delta u'_{RMS}(x, y, \phi)^2 \right\rangle_x}}, \tag{4.2}$$

are shown in figure 8(*d*) as a complement to the velocity traces. At the location closest to the wall ($y^+ = 40$), shown in figure 8(*c*), the periodic changes in residual turbulence are in phase with, but slightly lead, changes in the streamwise modal velocity. A similar phenomenon has also been reported for classical amplitude modulation effects measured in canonical high Reynolds number TBLs (Mathis *et al.* 2009). This is also reflected in figure 8(*d*), where there is a positive correlation between both modal velocity components and the residual turbulence near the wall, indicating that they are in phase. The spatial correlation between the streamwise modal velocity and residual turbulence ($R_u$ from (4.2)) is also analogous to the modulation coefficient denoted as $\Phi$ in (4.3), which is a phase-based correlation that has been used for single-point hot-wire measurements in Lozier *et al.* (2024*b*):

$$\Phi(y) = \frac{\left\langle \tilde{u}(x, y, \phi)\, \Delta u'_{RMS}(x, y, \phi) \right\rangle_\phi}{\sqrt{\langle \tilde{u}(x, y, \phi)^2 \rangle_\phi}\, \sqrt{\left\langle \Delta u'_{RMS}(x, y, \phi)^2 \right\rangle_\phi}}. \tag{4.3}$$

Agreement between $\Phi$ (blue asterisks) and $R_u$ (blue dotted line) across all wall-normal locations can be seen in figure 8(*d*), highlighting that these results do not depend on the specific measurement technique or correlation method (i.e. spatial versus temporal correlations). It is also noted that in previous experiments, the skewness magnitude for the actuated TBL was higher than the baseline canonical case in the near-wall and log-linear regions, supporting, broadly, an increase in inter-scale coupling under plasma forcing (Midya & Thomas 2025). The phase reversal reported for high Reynolds number canonical TBLs (Mathis *et al.* 2009) is not observed across the log-linear region here (figure 8*d*); however, there is a peak positive correlation between the residual turbulence and the wall-normal modal velocity $R_v$ in this region (which leads in phase; figure 8*b*). This suggests that both the large-scale wall-normal and streamwise motions may contribute to the observed modulation of streamwise turbulence intensity, depending on the wall-normal location. There is an eventual phase reversal (Mathis *et al.* 2009) and negative correlation between the streamwise modal velocity and residual turbulence, but only well above the actuator location, as shown in figures 8(*a*) and 8(*d*).

The streamwise and wall-normal components of the modal velocity are re-plotted in figures 9(*a*) and 9(*b*) where the wall-normal $y$-coordinate has been converted to inner-variable scaling, and the $y$-axis scale is logarithmic in order to better visualise the region of interest below the actuator. The minimum wall-normal distance shown in the maps in figure 9 is $y^+ = 30$. The map of streamwise residual turbulence downstream of the actuator is also re-plotted in figure 9(*c*), focusing attention on the region that is being modulated by the synthetic LSS, i.e. the near-wall TBL response to the imposed large-scale perturbation. The distinct shape or inclination of the modulated turbulence is apparent where the higher amplitude fluctuations occur near the log-linear region ($y^+ = 100$), and also occur farther downstream than the related fluctuations closer to the wall. It can also be seen that for a single pairing of negative and positive fluctuations in the residual turbulence (between $x = 6\delta$ and $x = 7\delta$, for instance), the transition from negative to positive amplitude in the upstream direction occurs over a shorter streamwise distance than the opposite transition from a positive to negative amplitude. This suggests that some nonlinear process may be contributing to the modulation in this region, otherwise the fluctuations in residual turbulence would be expected to follow a more evenly periodic shape, like that seen in the



Downloaded from https://www.cambridge.org/core. University of Notre Dame, on 05 Oct 2026 at 13:53:55, subject to the Cambridge Core terms of use, available at https://www.cambridge.org/core/terms. https://doi.org/10.1017/jfm.2026.12085

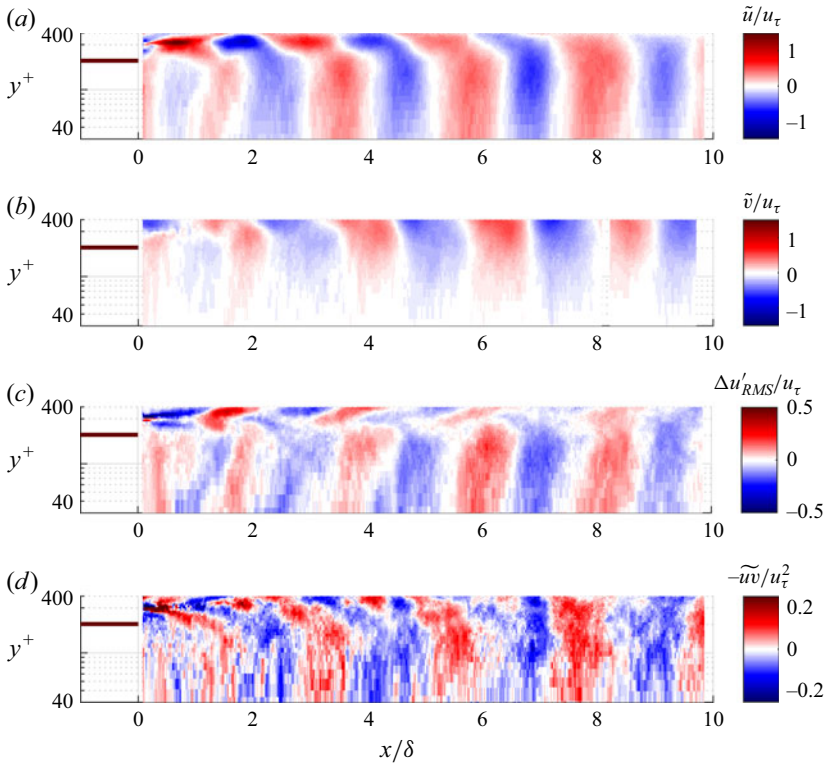



Figure 9. (*a*) Streamwise component of modal velocity. (*b*) Wall-normal component of modal velocity. (*c*) Streamwise component of residual turbulence. (*d*) Phase-locked Reynolds stress. Here, $H^+ = 200$, $f_p = 80$ Hz.

wall-normal modal velocity, for instance. The positive correlation between the residual turbulence and wall-normal modal velocity away from the wall can also be observed, suggesting that a wall-normal transport mechanism could also link the large-scale motions and the modulated turbulence in the log-linear region.

Phase-locked variations in the Reynolds stress have been re-plotted in figure 9(*d*). The strongest changes in the Reynolds stress are again concentrated around the log-linear region and have asymmetrical periodicity similar to that of the streamwise residual turbulence. In this case, the variations in the Reynolds stress appear to occur slightly upstream of the changes in the residual turbulence, or it could be said that peak Reynolds stress lags peak streamwise residual turbulence, but are in phase with changes in the streamwise modal velocity near the wall. A changing mean streamwise velocity gradient, due to the streamwise modal velocity fluctuations, and changes in Reynolds stress amplitude could be indications of a change in the local turbulence production near the wall, though the current measurements are not spatially resolved enough to directly measure this.

In Reynolds & Hussain (1972), a triple Reynolds decomposition was implemented to derive the governing dynamic equations describing the interaction between the mean flow, organised motions and turbulence. One term of interest for this research is the contribution to the turbulence production from the modal velocity components due to the synthetic vortical structures:



Downloaded from https://www.cambridge.org/core. University of Notre Dame, on 05 Oct 2026 at 13:53:55, subject to the Cambridge Core terms of use, available at https://www.cambridge.org/core/terms. https://doi.org/10.1017/jfm.2026.12085

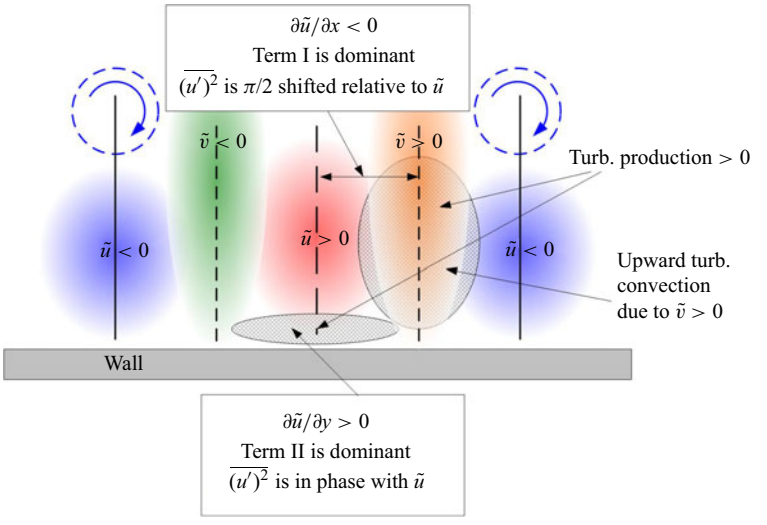



Figure 10. Schematic of the energy production due to the vortical structures induced by ALSSA. Vortical structures move from left to right.

$$\frac{\mathrm{D}}{\mathrm{D}t}\left(\overline{\frac{u_i' u_i'}{2}}\right) = \cdots - \overline{\langle u_i' u_j' \rangle \frac{\partial \tilde{u}_i}{\partial x_j}} \cdots , \tag{4.4}$$

where the overbar denotes time averaging, and the angled brackets denote phase averaging. For the case of the two-dimensional modal field, the contribution to the streamwise component fluctuation by the turbulent production becomes

$$\frac{\mathrm{D}}{\mathrm{D}t}\left(\overline{\frac{u'^2}{2}}\right) = \cdots - \underbrace{\overline{\langle u'^2 \rangle \frac{\partial \tilde{u}}{\partial x}}}_{\text{term I}} - \underbrace{\overline{\langle u'v' \rangle \frac{\partial \tilde{u}}{\partial y}}}_{\text{term II}} \cdots . \tag{4.5}$$

A schematic of the contribution to the streamwise component of the modal velocity due to the periodic vortical structure is presented in figure 10. The modal velocity is negative immediately below the vortical structure via the Biot–Savart mechanism (indicated as blue regions in figure 10), and is positive halfway between, or $\pi$-out-of-phase with, the adjacent structures (indicated as a red region in figure 10). This schematic is consistent with the experimental results presented in figure 6.

The dilatation-related term I in (4.5) is positive in the region where $\partial\tilde{u}/\partial x < 0$. From figure 10, it follows that the positive turbulence production related to term I is $\pi/2$ upstream of the vortical structure. As a consequence, the residual turbulence is $\pi/2$ out of phase with the modal $u$-component in the region below the actuator, which is, in this case, in the log-linear region. This is consistent with smaller values of $R_u$ (and the $\Phi$-modulation coefficient), which describes the phase difference between the residual turbulence and the streamwise modal velocity, in the log-linear region in figure 8($d$).

The shear-related term II in (4.5) is positive near the wall where $\partial\tilde{u}/\partial y > 0$, since $\langle u'v' \rangle < 0$. As at the wall $\tilde{u}(0) = 0$, in the near-wall region, $\partial\tilde{u}/\partial y \sim \tilde{u}$. This implies that the residual turbulence should be in phase with the streamwise component of the modal velocity near the wall, which is consistent with close-to-one values of the $\Phi$-modulation coefficient in the near-wall region in figure 8($d$). Finally, in addition to being produced, the turbulence is also transported upwards in the region where $\tilde{v} > 0$, as indicated in figure 10,



Downloaded from https://www.cambridge.org/core. University of Notre Dame, on 05 Oct 2026 at 13:53:55, subject to the Cambridge Core terms of use, available at https://www.cambridge.org/core/terms. https://doi.org/10.1017/jfm.2026.12085

extending the region of residual turbulence in the wall-normal direction, even above the location of the ALSSA; see figure 6(*d*) or figure 9(*c*).

These combined results then create a physical description of the relationship/interaction between the induced large-scale vortical motions in the outer region, and modulated turbulence intensities in the near-wall and log-linear regions. Large-scale motions induced by these vortices are superimposed onto the near-wall region through a linear process consistent with Biot–Savart induction. These superimposed large-scale motions, and their distinct spatial distribution, then lead to two regions of phase-dependent turbulence production, through different mechanisms. The induced large-scale wall-normal fluctuations are further responsible for the transport turbulence away from the wall, especially within the log-linear region. These combined turbulence production and transport mechanisms lead to the observed modulation of turbulence intensity in the near-wall and log-linear regions, which are in phase with the synthetic LSS. It is also noted that while the large-scale linear superposition and shear-related production mechanisms observed here are reminiscent of classical amplitude modulation effects, it is unclear if counterparts comparable to the wall-normal transport and dilatation-related production mechanisms exist for canonical LSS, as they are not typically associated with classical amplitude modulation effects. These result also motivate additional experiments, with greater spatial resolution, in order to measure these mechanisms of turbulence production and/or transport explicitly/independently.

We now investigate how these large-scale motions interact with, and/or change the characteristics of, the canonical near-wall structure/cycle. First, the phase speed of large-scale fluctuations was estimated by computing a streamwise spatial cross-correlation $R_x$ of the streamwise component of the modal velocity:

$$R_x(\Delta x,\, y,\, \phi,\, \Delta\phi) = \frac{\langle \tilde{u}(x,\, y,\, \phi)\, \tilde{u}(x+\Delta x,\, y,\, \phi+\Delta\phi)\rangle_x}{\sqrt{\langle \tilde{u}(x,\, y,\, \phi)^2\rangle_x}\,\sqrt{\langle \tilde{u}(x,\, y,\, \phi+\Delta\phi)^2\rangle_x}}. \tag{4.6}$$

A maximum in this streamwise spatial cross-correlation ($R_{x,max}$) represents the streamwise distance ($\Delta x$) that a large-scale fluctuation travels during the small time interval between two PIV measurements ($\Delta\phi\, T_P/2\pi$). As described in § 2, the PIV measurements resulted in five discrete phases (i.e. $\phi = n\pi/5$ with $n = 0, 2, 4, 6, 8$). As such, the cross-correlation was repeated for each of these distinct phases, with a fixed $\Delta\phi = 2\pi/5$, and then averaged to improve the cross-correlation estimate in each PIV measurement region. The streamwise displacement that results in a maximum in the cross-correlation, over a given time interval, can be used to determine the average phase speed of large-scale fluctuations over each measurement region:

$$u_{\phi PIV}(y) = \frac{\Delta x|_{R_x(\Delta x,y,\Delta\phi)=R_{x,max}}}{\Delta\phi\, T_P/2\pi}. \tag{4.7}$$

The results of this phase-speed analysis are shown in figure 11 as blue circles. There is good agreement in the estimated phase speed between the single-point hot-wire measurements and PIV across all streamwise locations, especially within the log-linear region of the boundary layer, as demonstrated in figure 11(*b*). In figure 11(*a*), above the actuator height, the phase speed of large-scale phase-locked fluctuations appears to be converging with the local mean velocity. Below the actuator height, the phase speed appears to be nearly constant, with a magnitude that is similar to the mean velocity at the location of the synthetic LSS (i.e. the actuator height). This observation indicates that fluctuations below the actuator are governed by the convection of the synthetic LSS produced in the outer region, rather than following the local dynamics (i.e. the local



Downloaded from https://www.cambridge.org/core. University of Notre Dame, on 05 Oct 2026 at 13:53:55, subject to the Cambridge Core terms of use, available at https://www.cambridge.org/core/terms. https://doi.org/10.1017/jfm.2026.12085

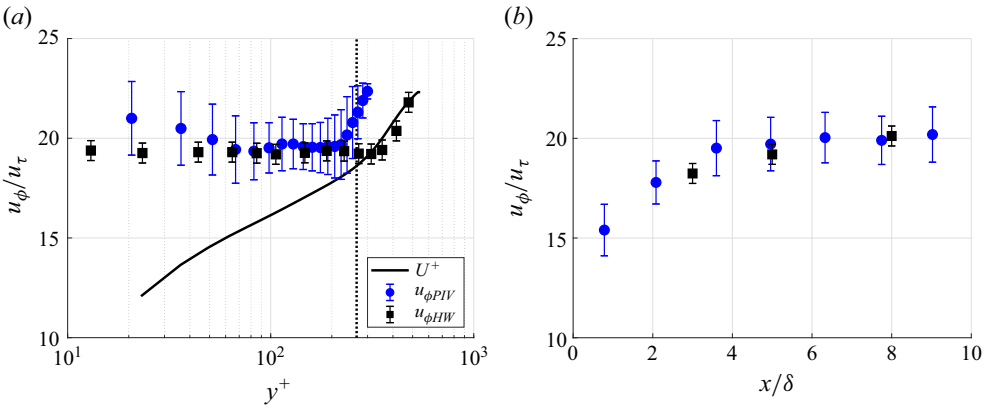



Figure 11. (*a*) Profiles of mean velocity (solid black line) and phase speed using a hot-wire from Lozier *et al.* (2024*b*) (black squares) and PIV (blue circles), with 90 % confidence intervals. Here, $x = 5\delta$. (*b*) Streamwise development of phase speed measured at $y^+ = 100$. Here, $H^+ = 200$, $f_p = 80$ Hz.

mean velocity), resulting in a travelling-wave-type effect. In figure 11(*b*), the phase speed around the log-linear region, $y^+ = 100$, appears to be reaching an asymptote by the farthest downstream locations. This phase-speed asymptote characterises the time scale of the boundary layer's adjustment to the presence of synthetic LSS, and corresponds well to the increasing magnitude of residual turbulence amplitudes observed in figure 7(*d*). This observation also motivates additional measurements over a larger downstream fetch, as the response of the TBL to the synthetic LSS evolves significantly over the present measurement domain. Additionally, the phase speed can be calculated using any phase-locked quantity, but in previous studies, they all showed the same trend (Lozier *et al.* 2024*b*), so the streamwise modal velocity was chosen here for simplicity.

To investigate what effect the synthetic LSS have on the spanwise organisation of near-wall structures and the dynamics of near-wall events, velocity correlations were computed using two spanwise-offset hot-wires. To quantify the spanwise correlation of the streamwise velocity between the two hot-wire probes, a standard two-point normalised correlation coefficient was computed:

$$R_z(x, y, \Delta z) = \frac{\overline{u(x, y, z, t)\, u(x, y, z + \Delta z, t)}}{\sqrt{\overline{u(x, y, z, t)^2}}\sqrt{\overline{u(x, y, z + \Delta z, t)^2}}}. \tag{4.8}$$

An example spanwise correlation coefficient profile for the canonical TBL (no actuator) obtained at $x/\delta = 8$ is shown in figure 12(*a*). In the log-linear region ($y^+ = 100$), the first crossing from positive to negative correlation is at approximately $\Delta z/\delta = 0.25$, which is consistent with the typical spanwise scale for $\delta$-scaled vortical structures (Tomkins & Adrian 2003; Ganapathisubramani *et al.* 2005). The data are plotted along with published results for a canonical boundary layer with low $Re_\tau$ from Ganapathisubramani *et al.* (2005), at a similar wall-normal location, and good agreement between the profiles is observed. The spanwise correlation coefficient profiles for the baseline canonical TBL across a range of wall-normal locations are shown in figure 12(*b*). Looking at the first zero-crossing of each profile, there is a clear growth in spanwise coherence, which is dependent on wall-normal location, from $y^+ = 25$ up to $y^+ = 350$ ($y/\delta = 0.5$), consistent with previous studies (Tomkins & Adrian 2003). Closer to the wall, the zero-crossing



Downloaded from https://www.cambridge.org/core. University of Notre Dame, on 05 Oct 2026 at 13:53:55, subject to the Cambridge Core terms of use, available at https://www.cambridge.org/core/terms. https://doi.org/10.1017/jfm.2026.12085

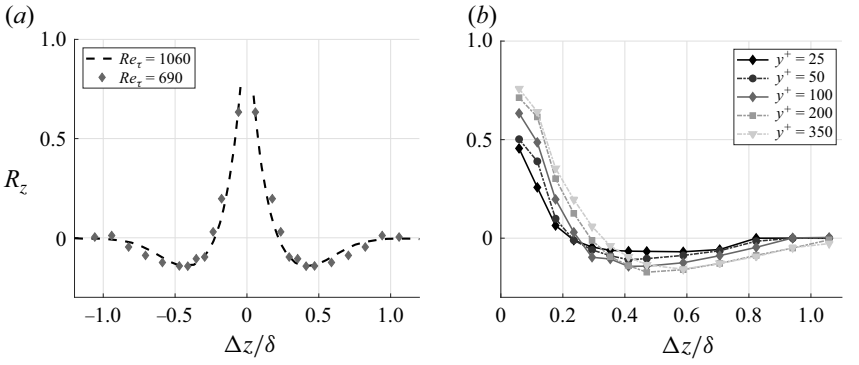



Figure 12. Spanwise profiles of the streamwise velocity correlation for the canonical TBL at (*a*) $y^+ = 100$ overlaid with data from Ganapathisubramani *et al.* (2005) ($Re_\tau = 1060$, $y^+ = 92$), and (*b*) a range of wall-normal locations, with lighter colours indicating greater distance from the wall. Here, $x = 8\delta$.

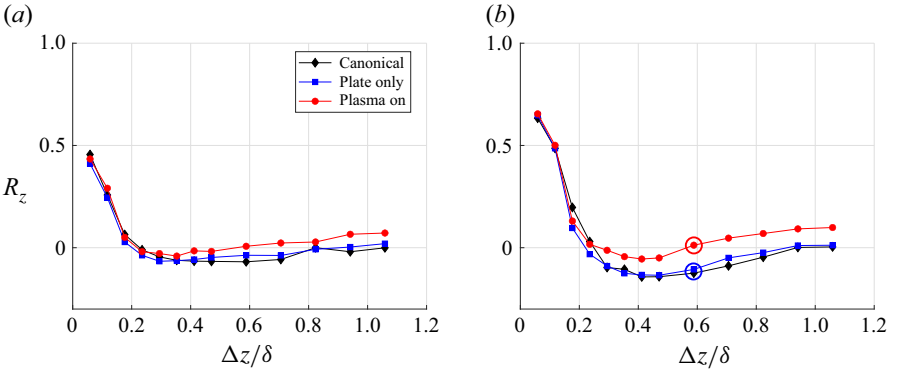



Figure 13. Spanwise profiles of streamwise velocity correlation for canonical, plate-only and plasma-on cases at (*a*) $y^+ = 25$ and (*b*) $y^+ = 100$. Circled points correspond to horizontal lines in figure 14. Here, $H^+ = 200$, $x = 8\delta$, $f_P = 80$ Hz.

is approaching the reported value $\Delta z^+ = 100$ ($\Delta z/\delta = 0.15$), which corresponds to the distribution of canonical near-wall structures (Antonia & Bisset 1990).

Spanwise correlations for the canonical, plate-only and plasma-on cases in the near-wall and log-linear regions are compared in figure 13. At both wall-normal locations, the addition of the actuator plate alone does not result in a modification of the level of spanwise correlation as compared to the canonical case. However, when the plasma forcing is active, there is a positive shift in the spanwise correlation, even at the largest separation distances. In both locations, but specifically in the log-linear region, the first zero-crossing of the profile does not change location, indicating that there is no net effect of the actuator plate or plasma forcing on the spanwise organisation of small-scale vortical structures.

However, this correlation is an average measure, and in the case of active plasma forcing, it is useful to decompose the velocity time series that has been phase-locked to the plasma forcing. Using the phase-locked decomposition method shown earlier, a phase-dependent



Downloaded from https://www.cambridge.org/core. University of Notre Dame, on 05 Oct 2026 at 13:53:55, subject to the Cambridge Core terms of use, available at https://www.cambridge.org/core/terms. https://doi.org/10.1017/jfm.2026.12085

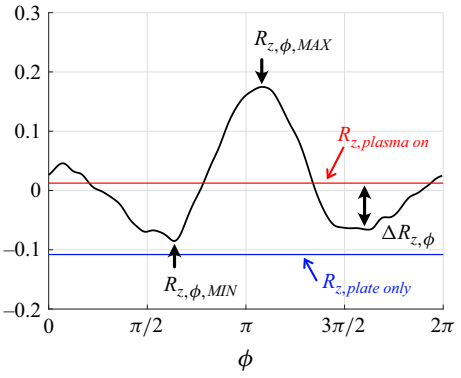



Figure 14. Phase-dependent variation in spanwise correlation, with $\Delta z = 0.6\delta$ for the plasma-on case at $y^+ = 100$. Horizontal lines correspond to circled points in figure 13(*b*). Here, $H^+ = 200$, $x = 8\delta$, $f_P = 80$ Hz.

two-point correlation coefficient was also computed:

$$R_{z,\phi}(y, \Delta z, \phi) = \frac{\langle u(y, z, \phi, n)\, u(y, z + \Delta z, \phi, n)\rangle_n}{\sqrt{\langle u(y, z, \phi, n)\rangle_n^2}\,\sqrt{\langle u(y, z + \Delta z, \phi, n)\rangle_n^2}}. \tag{4.9}$$

As a final step, similar to the residual turbulence, the phase average of this phase-dependent correlation was removed in order to analyse phase-dependent changes in the spanwise correlation, later labelled $\Delta R_{z,\phi}$ (figure 14). A phase-locked measurement of the spanwise correlation in the log-linear region ($y^+ = 100$) for a single spanwise separation distance is shown in figure 14. The average spanwise correlations for the plasma-on and plate-only cases are shown as horizontal lines, which correspond to the circled points in figure 13(*b*). The peak in the phase-dependent spanwise correlation ($R_{z,\phi,MAX}$), and minimum ($R_{z,\phi,MIN}$), were identified as shown in figure 14. Comparison with figures 7(*b*) and 7(*d*) reveals that the maximum in the phase-dependent spanwise correlation is aligned with negative fluctuations in both the streamwise modal velocity and residual turbulence. Additionally, the maximum spanwise correlation occurs just upstream of – i.e. a phase lag with respect to – the synthetic LSS passing in the outer region.

The maximum and minimum amplitudes of the spanwise correlation can then be computed across all spanwise separation distances, and used to isolate effects relative to the passing of the synthetic LSS in the outer region. These results are shown in figure 15 for the streamwise location $x = 8\delta$ downstream of the actuator. Even sufficiently far downstream, the synthetic LSS still have a significant effect on the spanwise correlation as they pass through, demonstrated by the red dotted lines ($R_{z,\phi,MAX}$) in figure 15. However, after the synthetic LSS move slightly downstream, the correlation magnitudes relax back to canonical (or plate-only) levels, as shown by the dashed blue lines ($R_{z,\phi,MIN}$, which can also be seen in figure 14). These localised increases in the spanwise correlation (compared to the canonical/plate-only magnitudes) over large spanwise separations suggest that the spanwise-uniform, synthetic, large-scale motions induced by the actuator become dominant flow features of the near-wall and log-linear regions as the synthetic LSS convect past a streamwise location. Additionally, phases associated with dominant spanwise-uniform motions are also associated with a decrease in the residual turbulence, consistent with the model of Schoppa & Hussain (2002). But this influence is also transient, as the canonical spanwise correlation profile is recovered in between each passing. These combined phase-speed and spanwise correlation results suggest that locally there are



Downloaded from https://www.cambridge.org/core. University of Notre Dame, on 05 Oct 2026 at 13:53:55, subject to the Cambridge Core terms of use, available at https://www.cambridge.org/core/terms. https://doi.org/10.1017/jfm.2026.12085

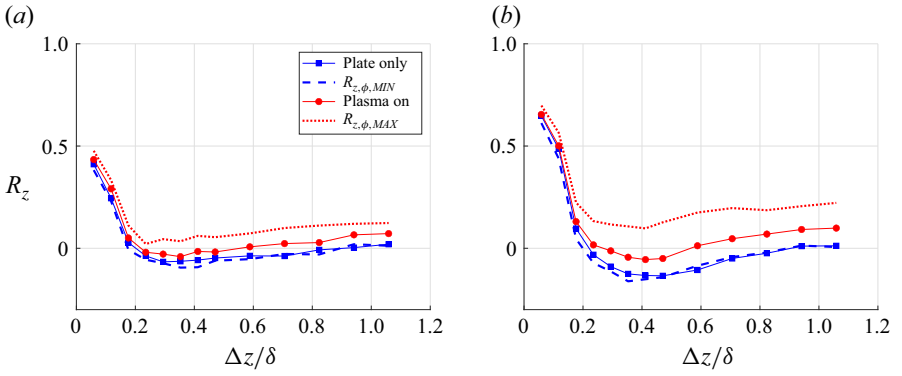



Figure 15. Spanwise profiles of streamwise velocity correlation for plate-only and plasma-on cases at (*a*) $y^+ = 25$ and (*b*) $y^+ = 100$. Maximum and minimum phase-dependent correlations are shown as dashed and dotted lines, respectively. Here, $H^+ = 200$, $x = 8\delta$, $f_P = 80$ Hz.

changes to the near-wall structure dynamics as the induced spanwise-uniform large-scale motions travel through the near-wall region; however, there is no lasting modification of the near-wall structure as seen from the spanwise correlation recovery. This is further supported by Midya & Thomas (2025), where both the frequency and intensity of near-wall bursting events were found to vary over the actuation cycle, with little net effect.

## 5. Conclusions and discussion

An active plasma-based actuator was used to introduce periodic, spanwise-uniform, large-scale vortical structures into the outer region of a canonical turbulent boundary layer (TBL). The Reynolds number of this canonical TBL was also kept sufficiently low so that naturally occurring energetic large-scale structures (LSS) were not present in the outer region (as evidenced by the premultiplied 1-D wavenumber energy spectra). In this manner, the interactions/influence of these imposed, idealised, outer-region motions (called synthetic LSS here) on the global TBL dynamics could be effectively observed.

Planar PIV and spanwise offset hot-wires were used to study the development of the synthetic LSS as well as the TBL's response to this imposed large-scale perturbation. Spatially resolved PIV measurements showed that downstream of the actuator, spanwise vortices generated by the actuator induced coherent streamwise and wall-normal velocity fluctuations in the log-linear and near-wall regions through a linear process that is fully consistent with Biot–Savart induction. These induced, superimposed, large-scale motions were also found to be directly correlated with local, phase-dependent modulation of the small-scale turbulence intensity (with correlation characteristics/magnitudes comparable to other actuation schemes, such as in McKeon *et al.* (2018), and classical amplitude modulation effects). Measurements indicate that the modulation of turbulence amplitudes here was associated with an imposed periodic variation in turbulence production, associated with both the wall-normal modal strain rate ($\partial\tilde{u}/\partial y$) and the dilatational modal strain rate ($\partial\tilde{u}/\partial x$), as well as wall-normal turbulence transport associated with the wall-normal modal velocity component ($\tilde{v}$). It is noted that while these superposition and shear-related production mechanisms are also attributed to canonical TBLs (i.e. consistent with classical amplitude modulation effects), it remains unclear if the observed wall-normal transport and/or dilatation-related production mechanisms will have comparable counterparts in canonical TBLs due to the idealised nature of the outer–inner interaction



Downloaded from https://www.cambridge.org/core. University of Notre Dame, on 05 Oct 2026 at 13:53:55, subject to the Cambridge Core terms of use, available at https://www.cambridge.org/core/terms. https://doi.org/10.1017/jfm.2026.12085

investigated here (i.e. these mechanisms are not typically associated with the naturally occurring LSS found in higher Reynolds number canonical TBLs).

Additionally, the phase speed of these induced large-scale motions was found to be nearly constant below the actuator, at $u_\phi \approx 0.84U_\infty$, which corresponds directly to the measured convection velocity of the synthetic LSS in the outer region. Measurements of the spatial coherence of streamwise velocity fluctuations also showed that in the presence of the synthetic LSS, the induced spanwise-uniform streamwise modal velocity fluctuations were a dominant feature of the flow, as evidenced by a significant positive shift in the spanwise spatial correlation, even at the largest probe separation distances. These induced spanwise-uniform streamwise modal velocity fluctuations were also shown to be locally correlated with the phase-dependent modulation of turbulence intensity and the amplitude and frequency of bursting events (Midya & Thomas 2025), collectively confirming an influence of the outer-region synthetic LSS on the near-wall dynamics. However, in both the near-wall and log-linear regions, the first zero-crossing of the correlation profile did not change in spanwise offset, and the correlation profile was found to relax back to canonical levels during phases of the actuation cycle corresponding to the synthetic LSS moving downstream from the measurement location, indicating that there is no sustained effect of the outer-region synthetic LSS on the spanwise organisation of smaller-scale vortical/streak structures near the wall. This is also reflected in the time-averaged streamwise turbulence intensity near the wall, which did not change significantly under plasma forcing for streamwise locations $x \lesssim 8\delta$. While these results collectively reflect a significant and measurable influence of the imposed, outer-region, synthetic LSS on the near-wall turbulence dynamics, as expected, a lack of sustained alteration to the near-wall structure suggests that it largely retains its autonomous character between the observed intermittent interactions with the idealised motions/perturbation imposed here.

Additionally, these results/conclusions were found to be consistent with the previous work of Liu *et al.* (2022) and Lozier *et al.* (2024*b*), and the complementary study of Midya & Thomas (2025), which further examined the skewness of the streamwise velocity fluctuations as a function of frequency (scale) in both the canonical and the actuated TBL under consideration here. The intimate connection between skewness and inter-scale interactions in canonical TBLs was previously characterised by Mathis *et al.* (2009, 2011*b*) and Lozier *et al.* (2024*a*). For instance, in these studies, a normalised correlation coefficient, between low-pass filtered velocity signals in the outer region and the envelope of near-wall small-scale velocity fluctuations obtained via a Hilbert transform, was found to bear a very strong resemblance to the corresponding velocity skewness profile. As such, using bispectral methods (Rosenblatt & Van Ness 1965; Elgar & Guza 1985), the spectral distribution of skewness contributing scales for the plasma-on and canonical boundary layers, presented in this work, were calculated and compared at selected wall-normal locations in Midya & Thomas (2025). In the log-linear region ($y^+ = 60$), the spectral distributions of the skewness were found to be distinctly different for the plasma-on and canonical TBLs, suggesting non-trivial changes in the inter-scale interactions in this region attributed to the outer-region synthetic LSS. However, in the near-wall region ($y^+ = 8$ and 15), there remained a strong resemblance between the spectral distributions of the plasma-on and canonical cases supporting the persistence of an autonomous structure/cycle in the near-wall region (consistent with the conclusions of the present study). These skewness analyses then further confirm that while there is a clear and measurable influence of the imposed outer-region synthetic LSS, through interaction with the superimposed large-scale motions and modulation of turbulence amplitudes/dynamics (i.e. frequency and amplitude of bursting events), the canonical autonomous near-wall structures/mechanisms remain dominant and largely intact.



Downloaded from https://www.cambridge.org/core. University of Notre Dame, on 05 Oct 2026 at 13:53:55, subject to the Cambridge Core terms of use, available at https://www.cambridge.org/core/terms. https://doi.org/10.1017/jfm.2026.12085

Downloaded from https://www.cambridge.org/core. University of Notre Dame, on 05 Oct 2026 at 13:53:55, subject to the Cambridge Core terms of use, available at https://www.cambridge.org/core/terms. https://doi.org/10.1017/jfm.2026.12085



These results also have implications regarding the design and optimisation of future flow control techniques. While the present results indicate that transient changes in the near-wall turbulence amplitude/dynamics can be achieved through the introduction of large-scale perturbations in the outer region, there is also a limitation in achieving sustained modification of near-wall structures/mechanisms, especially compared to actuation done at (or near) the wall (Marusic *et al.* 2021; Meyers *et al.* 2025). These results also motivate additional experiments to connect the processes of the idealised outer–inner interaction described here (i.e. for a spanwise-uniform large-scale perturbation in the outer region) with the processes that lead to classical amplitude modulation effects in the near-wall region of canonical TBLs (i.e. from the more complex canonical LSS topography). This could involve novel actuation strategies that replicate additional characteristics of the canonical LSS, such as their inherently stochastic and three-dimension distribution (i.e. meandering groups/packets of hairpin-like vortices) and/or manipulating higher Reynolds number baseline TBLs that contain naturally occurring energetic large-scale motions and a well-established log-linear region.

**Acknowledgements.** The authors would like to thank Dr I. Gluzman for his help in setting up and aligning the PIV system.

**Funding.** This research was funded by the Office of Naval Research, grant N00014-18-1-2534.

**Declaration of interests.** The authors report no conflict of interest.

## References

Adrian, R.J. 2007 Hairpin vortex organization in wall turbulence. *Phys. Fluids* **19** (4), 041301.

Adrian, R.J., Meinhart, C.D. & Tomkins, C.D. 2000 Vortex organization in the outer region of the turbulent boundary layer. *J. Fluid Mech.* **422**, 1–54.

Alfredsson, P.H. & Örlü, R. 2018 Large-eddy breakup devices – a 40 years perspective from a Stockholm horizon. *Flow Turbul. Combust.* **100** (4), 877–888.

Andreolli, A., Gatti, D., Vinuesa, R., Örlü, R. & Schlatter, P. 2023 Separating large-scale superposition and modulation in turbulent channels. *J. Fluid Mech.* **958**, A37.

Antonia, R.A. & Bisset, D.K. 1990 Spanwise structure in the near-wall region of a turbulent boundary layer. *J. Fluid Mech.* **210**, 437–458.

Bandyopadhyay, P.R. & Hussain, A.K.M.F. 1984 The coupling between scales in shear flows. *Phys. Fluids* **27** (9), 2221.

Chan, C.I., Örlü, R., Schlatter, P. & Chin, R.C. 2022 Large-scale and small-scale contribution to the skin friction reduction in a modified turbulent boundary layer by a large-eddy break-up device. *Phys. Rev. Fluids* **7** (3), 034601.

Chen, X., Iwano, K., Sakai, Y. & Ito, Y. 2021 Effect of large-scale structures on bursting phenomenon. *Intl J. Heat Fluid Flow* **89**, 108811.

Cheng, X.Q., Wong, C.W., Hussain, F., Schroder, W. & Zhou, Y. 2021 Flat plate drag reduction using plasma-generated streamwise vortices. *J. Fluid Mech.* **918**, A24.

Chernyshenko, S.I., Marusic, I. & Mathis, R. 2012 Quasi-steady description of modulation effects in wall turbulence. arXiv: 1203.3714 [physics.flu-dyn].

Corke, C., Nagib, H.M. & Guezennec, Y. 1982 A new view on origin, role and manipulation of large scales in turbulent boundary layers. *Tech. Rep.* NASA-CR-165861. Illinois Institute of Technology.

Corke, T.C. & Thomas, F.O. 2018 Active and passive turbulent boundary-layer drag reduction. *AIAA J.* **56** (10), 3835–3847.

Dowling, A.P. 1985 The effect of large-eddy breakup devices on oncoming vorticity. *J. Fluid Mech.* **160**, 447–463.

Duong, A.H., Corke, T.C. & Thomas, F.O. 2021 Characteristics of a drag-reduced turbulent boundary layer with pulsed-direct-current plasma actuation. *J. Fluid Mech.* **915**, A113.

Duvvuri, S. & McKeon, B.J. 2015 Triadic scale interactions in a turbulent boundary layer. *J. Fluid Mech.* **767**, R4.

Elgar, S. & Guza, R.T. 1985 Observations of bispectra of shoaling surface gravity waves. *J. Fluid Mech.* **161**, 425–448.

GANAPATHISUBRAMANI, B., HUTCHINS, N., HAMBLETON, W.T., LONGMIRE, E.K. & MARUSIC, I. 2005 Investigation of large-scale coherence in a turbulent boundary layer using two-point correlations. *J. Fluid Mech.* **524**, 57–80.

GUALA, M., HOMMEMA, S.E. & ADRIAN, R.J. 2006 Large-scale and very-large-scale motions in turbulent pipe flow. *J. Fluid Mech.* **554**, 521–542.

HAMILTON, J.M., KIM, J. & WALLEFE, F. 1995 Regeneration mechanisms of near-wall turbulence sturctures. *J. Fluid Mech.* **287**, 317–348.

HUNT, J.C.R. & MORRISON, J.F. 2000 Eddy structure in turbulent boundary layers. *Eur. J. Mech. B/Fluids* **19**, 673–694.

HUTCHINS, N. & MARUSIC, I. 2007*a* Evidence of very long meandering features in the logarithmic region of turbulent boundary layers. *J. Fluid Mech.* **579**, 1–28.

HUTCHINS, N. & MARUSIC, I. 2007*b* Large-scale influences in near-wall turbulence. *Phil. Trans. R. Soc. A: Math. Phys. Engng Sci.* **365** (1852), 647–664.

HUTCHINS, N., NICKELS, T.B., MARUSIC, I. & CHONG, M.S. 2009 Hot-wire spatial resolution issues in wall-bounded turbulence. *J. Fluid Mech.* **635**, 103–136.

HUYNH, D. & MCKEON, B. 2020 Characterization of the spatio-temporal response of a turbulent boundary layer to dynamic roughness. *Flow Turbul. Combust.* **104** (2–3), 293–316.

JEONG, J. & HUSSAIN, F. 1995 On the identification of a vortex. *J. Fluid Mech.* **285**, 69–94.

JIMÉNEZ, J., HOYAS, S., SIMENS, M.P. & MIZUNO, Y. 2010 Turbulent boundary layers and channels at moderate Reynolds numbers. *J. Fluid Mech.* **657**, 335–360.

JIMÉNEZ, J. & PINELLI, A. 1999 The autonomous cycle of near-wall turbulence. *J. Fluid Mech.* **389**, 335–359.

KIM, J. 2011 Physics and control of wall turbulence for drag reduction. *Phil. Trans. R. Soc. A: Math. Phys. Engng Sci.* **369**, 1396–1411.

KIM, J.-S., HWANG, J., YOON, M., AHN, J. & SUNG, H.J. 2017 Influence of a large-eddy breakup device on the frictional drag in a turbulent boundary layer. *Phys. Fluids* **29** (6), 065103.

KLEWICKI, J., FIFE, P., WEI, T. & MCMURTRY, P. 2007 A physical model of the turbulent boundary layer consonant with mean momentum balance structure. *Phil. Trans. R. Soc. A: Math. Phys. Engng Sci.* **365** (1852), 823–840.

KLINE, S.J., REYNOLDS, W.C., SCHRAUB, F.A. & RUNSTADLER, P.W. 1967 The structure of turbulent boundary layers. *J. Fluid Mech.* **30** (4), 741–773.

LIU, C., GLUZMAN, I., LOZIER, M., MIDYA, S., GORDEYEV, S., THOMAS, F.O. & GAYME, D.F. 2022 Spatial input–output analysis of actuated turbulent boundary layers. *AIAA J.* **60** (11), 6313–6327.

LIU, X., THOMAS, F.O. & NELSON, R.C. 2002 An experimental investigation of the planar turbulent wake in constant pressure gradient. *Phys. Fluids* **14** (8), 2817–2838.

LOZIER, M. 2023 Characterization of turbulent boundary layer dynamics via active manipulation of large-scale structures. PhD thesis, University of Notre Dame.

LOZIER, M., THOMAS, F.O. & GORDEYEV, S. 2023 Experimental investigation of turbulent boundary layer dynamics via active manipulation of large-scale structures. *Intl J. Heat Fluid Flow* **103**, 109194.

LOZIER, M., MARUSIC, I. & DESHPANDE, R. 2024*a* Revisiting amplitude modulation in non-canonical wall-turbulence through high-Reynolds number experimental data. *Phys. Rev. Fluids* **9**, 124602.

LOZIER, M., THOMAS, F.O. & GORDEYEV, S. 2024*b* Response of a turbulent boundary layer to an imposed synthetic large-scale structure. *AIAA J.* **62** (2), 573–589.

LUCHIK, T.S. & TIEDERMAN, W.G. 1987 Timescale and structure of ejections and bursts in turbulent channel flows. *J. Fluid Mech.* **174**, 529–552.

MARUSIC, I., CHANDRAN, D., ROUHI, A., FU, M.K., WINE, D., HOLLOWAY, B., CHUNG, D. & SMITS, A.J. 2021 An energy-efficient pathway to turbulent drag reduction. *Nat. Commun.* **12** (1), 5805.

MARUSIC, I. & MONTY, J.P. 2019 Attached eddy model of wall turbulence. *Annu. Rev. Fluid Mech.* **51** (1), 49–74.

MATHIS, R., HUTCHINS, N. & MARUSIC, I. 2009 Large-scale amplitude modulation of the small-scale structures in turbulent boundary layers. *J. Fluid Mech.* **628**, 311–337.

MATHIS, R., HUTCHINS, N. & MARUSIC, I. 2011*a* A predictive inner–outer model for streamwise turbulence statistics in wall-bounded flows. *J. Fluid Mech.* **681**, 537–566.

MATHIS, R., MARUSIC, I., CHERNYSHENKO, S.I. & HUTCHINS, N. 2013 Estimating wall-shear-stress fluctuations given an outer region input. *J. Fluid Mech.* **715**, 163–180.

MATHIS, R., MARUSIC, I., HUTCHINS, N. & SREENIVASAN, K.R. 2011*b* The relationship between the velocity skewness and the amplitude modulation of the small scale by the large scale in turbulent boundary layers. *Phys. Fluids* **23** (12), 121702.

MCKEON, B.J., JACOBI, I. & DUVVURI, S. 2018 Dynamic roughness for manipulation and control of turbulent boundary layers: an overview. *AIAA J.* **56** (6), 2178–2193.



Downloaded from https://www.cambridge.org/core. University of Notre Dame, on 05 Oct 2026 at 13:53:55, subject to the Cambridge Core terms of use, available at https://www.cambridge.org/core/terms. https://doi.org/10.1017/jfm.2026.12085

MEYERS, A., DUONG, A., CORKE, T.C. & THOMAS, F.O. 2025 Characterizing turbulent boundary layer response and recovery to buffer layer spanwise blowing. *J. Fluid Mech.* **1016**, A26.

MIDYA, S. & THOMAS, F. 2025 Decomposition of streamwise velocity skewness in zero-pressure-gradient canonical and actuated turbulent boundary layers. *Phys. Rev. Fluids* **10**, 114606.

PANTON, R.L. 2001 Overview of the self-sustaining mechanisms of wall turbulence. *Prog. Aerosp. Sci.* **37** (4), 341–383.

RANADE, P., DUVVURI, S., MCKEON, B.J., GORDEYEV, S., CHRISTENSEN, K. & JUMPER, E.J. 2019 Turbulence amplitude amplification in an externally forced, subsonic turbulent boundary layer. *AIAA J.* **57** (9), 3838–3850.

REYNOLDS, W.C. & HUSSAIN, A.K.M.F. 1972 The mechanics of an organized wave in turbulent shear flow. Part 3. Theoretical models and comparisons with experiments. *J. Fluid Mech.* **54** (2), 263–288.

ROBINSON, S.K. 1991 Coherent motions in the turbulent boundary layer. *Annu. Rev. Fluid Mech.* **23**, 601–639.

ROSENBLATT, M. & VAN NESS, J.W. 1965 Estimation of the bispectrum. *Ann. Math. Stat.* **36** (4), 1120–1136.

SAVILL, A.M. & MUMFORD, J.C. 1988 Manipulation of turbulent boundary layers by outer-layer devices: skin-friction and flow-visualization results. *J. Fluid Mech.* **191**, 389–418.

SCHOPPA, W. & HUSSAIN, F. 2002 Coherent structure generation in near-wall turbulence. *J. Fluid Mech.* **453**, 57–108.

DE SILVA, C.M., HUTCHINS, N. & MARUSIC, I. 2016 Uniform momentum zones in turbulent boundary layers. *J. Fluid Mech.* **786**, 309–331.

SMITS, A.J., MCKEON, B.J. & MARUSIC, I. 2011 High-Reynolds number wall turbulence. *Annu. Rev. Fluid Mech.* **43** (1), 353–375.

SPENCER, M., KALENSKY, M., GORDEYEV, S. & KEMNETZ, M. 2024 Aero-optical effects, part II. Sources of aberrations: tutorial. *J. Opt. Soc. Am. A* **41**, 2175–2187.

THOMAS, F.O., CORKE, T.C. & DUONG, A.H. 2023 Airfoil friction drag reduction with net power savings using pulsed-direct-current plasma actuation. *AIAA J.* **61** (9), 4045–4055.

THOMAS, F.O., CORKE, T.C., DUONG, A., MIDYA, S. & YATES, K. 2019 Turbulent drag reduction using pulsed-DC plasma actuation. *J. Phys. D: Appl. Phys.* **52**, 434001.

THOMAS, F.O., CORKE, T.C., IQBAL, M., KOZLOV, A. & SCHATZMAN, D. 2009 Optimization of dielectric barrier discharge plasma actuators for active aerodynamic flow control. *AIAA J.* **47** (9), 2169–2178.

TOMKINS, C.D. & ADRIAN, R.J. 2003 Spanwise structure and scale growth in turbulent boundary layers. *J. Fluid Mech.* **490**, 37–74.



Downloaded from https://www.cambridge.org/core. University of Notre Dame, on 05 Oct 2026 at 13:53:55, subject to the Cambridge Core terms of use, available at https://www.cambridge.org/core/terms. https://doi.org/10.1017/jfm.2026.12085